Catalytic and Photocatalytic Properties of Oxide Spinels

Tetiana Tatarchuk, Basma Al-Najar, Mohamed Bououdina, and Mamdouh Abdel Aal Ahmed

Contents

T. Tatarchuk (✉)
Department of Chemistry, Faculty of Natural Science, Vasyl Stefanyk Precarpathian National University, Ivano-Frankivsk, Ukraine

Educational and Scientific Center of Materials Science and Nanotechnology, Vasyl Stefanyk Precarpathian National University, Ivano-Frankivsk, Ukraine
e-mail: tatarchuk.tetyana@gmail.com

B. Al-Najar · M. Bououdina
Department of Physics, College of Science, University of Bahrain, Zallaq, Bahrain
e-mail: balnajar85@gmail.com; mboudina@gmail.com

M. A. A. Ahmed
Physics Department, Faculty of Science, Al Azhar University, Nasr City, Cairo, Egypt
e-mail: mamdouh_2000_2000@yahoo.com

L. M. T. Martínez et al. (eds.), *Handbook of Ecomaterials*,
https://doi.org/10.1007/978-3-319-48281-1_158-1

Abstract

Oxide spinels (OSs) have been identified as perspective functional materials in various fields of applications including water treatment, degradation of dyes, hyperthermia, and drug delivery and as antibacterial agent. In recent years, extensive researches are devoted to the synthesis and properties of spinel nano-oxide systems to fulfill the essential requirement of better chemical and thermal stabilities with enhanced catalytic and photocatalytic. In this chapter, the applications of OSs (ferrites, aluminates, chromites) as heterogeneous catalysts in different inorganic processes and as photocatalysts in many chemical processes such as decomposition, oxidation, reduction, and construction are described. The catalytic properties of OSs crucially depend on the distribution of cations among the octahedral and tetrahedral sites in the spinel structure and accordingly the corresponding physical properties. In particular, the most interesting feature of spinel ferrites is the magnetic property for the removal of catalyst from the reaction medium by means of a magnet without loss of catalytic or photocatalytic activities. These compounds have well-established catalytic characteristics for many reactions including carbon monoxide oxidation, catalytic decomposition of greenhouse gases (CO_2, N_2O, CH_4), catalytic combustion (oxidation) of soot, and the growth of the CNTs. Through this chapter, we hope to provide the readers with a distinct perspective of the present and future of this field.

Keywords

Catalyst · Active center · Mössbauer spectroscopy · Photocatalysis · Spinel · Ferrite · Soot · Dye · Catalytic activity

Introduction

The oxide spinels of general formula AB_2O_4, where A and B are divalent and trivalent metallic cations, respectively, are widely used as magnetic materials [1–6], catalysts and photocatalysts [7–9], adsorbents [10], biosensors systems [11, 12], contrast agents in magnetic resonance imaging (MRI) [13], antimicrobial systems [14], cancer treatment [15], drug delivery [16], and so on. Ferrospinels have been very often used as cores for various catalytic shells [17]. Such catalysts have advantages, as they could be easily magnetically separated from the reaction system. Core-shell nanomaterials are found to possess better catalytic activity due to the presence of different effects (ligand, ensemble, and geometric). Magnetically separable ferrite nanoparticles can also be used as Fenton catalysts for the removal of several types of pollutants.

The oxide spinels have tunable physical and chemical properties and thus can be synthesized in any specific size and geometry depending on their desired application. In the spinel-type compounds, divalent and trivalent ions can occupy octahedral and tetrahedral sites within the crystal lattice. The possibility of the presence of metal cations in tetrahedral and octahedral positions leads to the surface heterogeneity and

often influences the catalytic activity. The results reported by many recent studies indicate that in catalysis, the activity of oxide catalysts depends on many factors such as the method of synthesis and precursors. Also, it was found that mixed oxide systems used in many catalytic reactions are more active than their separate components. Many reports have shown correlation between structural parameters (cations present in octahedral and tetrahedral sites) and the catalytic activity of spinel compounds. Jacobs et al. [18] established that, in oxide spinels, the catalytic activity was mainly due to octahedral cations.

Many researches showed that heterogeneous catalytic reactions occurred at the active sites of spinel catalyst surface [19]. The catalytic activity and selectivity of catalyst depend on the nature of atom's active centers, method of catalyst preparation, chemical composition and cationic distribution between crystal sub-lattice, etc. [20]. This chapter provides the readers with in-depth information about different oxide spinel compounds which have well-established catalytic characteristics for many reactions.

Structure and Physicochemical Properties of Spinel Compounds

Oxide spinels as non-noble nanocatalysts used in various catalysis fields, including photocatalysis, have been recently widely investigated due to their low cost, high reactivity, and low toxicity. Among them, Fe-based catalysts are very popular. Mössbauer spectroscopy is a powerful technique that gives information about ferric or ferrous ions taking part in the catalysis process and investigates the possibility of any correlation between catalytic behavior and the coordination structure of catalysts, which are highly desirable for clarifying the involved mechanisms [21, 22]. The knowledge of the local electronic structure, identifying the active site, determining the crystal phase, and tracking the oxidation state and environment change of various Fe-based catalysts with the application of Mössbauer technique, is of great importance for the further development in these catalysis fields [21].

^{57}Fe Mössbauer spectroscopy as a nuclear probe technique in solids is based on the nuclear resonant absorption and emission of gamma rays which provides deep insight on the atomistic nature of different materials (ca. spinel ferrites). This resonance effect was discovered in 1958 by Professor Rudolf Mössbauer, who received the Nobel Prize in Physics in 1961. Since the early days of Mössbauer spectroscopy (MS), a vast amount of work on spinel ferrites has been published. As early as the first decade of Mössbauer, 1961–1970, the first Mössbauer measurements on the spinel ferrite γ-Fe_2O_3 were carried out by Bauminger et al. [23] and Kelly et al. [24]. For $CuFe_2O_4$, the first results were reported by Evan et al. [25].

Fortunately, on 1968, an interesting review article was published by Evans [26] on the magnetic hyperfine interactions in some spinel ferrites. He claimed that finer details of ^{57}Fe data in ferritic spinels can be explained by the super transferred hyperfine interaction mechanisms. The Fe^{3+}-O^{2-} distance is substantially different for A and B sites in the spinels, and the number of magnetic neighbors is also different for the two sites being 6 for B site and 12 for the A site. These two factors

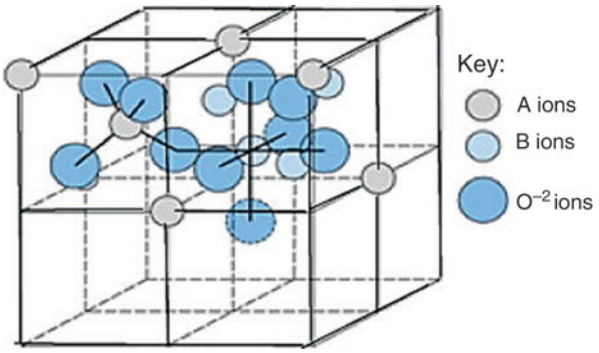

Fig. 1 Two octants of the spinel unit cell showing A-ions in the tetrahedral sites and B-ions in the octahedral sites

alone would lead to the required difference in the influence of a given ion on the A-site and B-site fields. For many material scientists, there is an increase need for a better understanding of this Mössbauer spectroscopy (MOS) and its underlying principles. This chapter contains some elementary notes of MOS in characterizing the spectrum of iron in spinel ferrite in the level of nanoscale. Figure 1 shows the unit cell of normal spinel ferrite $MeFe_2O_4$ (Me is divalent metal cation).

The crystal structure of spinel ferrites is fairly formulated as $(Me_{1-x}Fe_x)[Me_xFe_{2-x}]O_4$, where parentheses enclose cations in tetrahedral (A) coordination and square brackets denote octahedral [B] cation sites [27], while x represents the degree of inversion which is meant either the fraction of (A) sites occupied by Fe^{3+} cations or the fraction of [B] sites occupied by Me^{2+} cations. It is widely appreciated that the degree of inversion in spinel ferrites gives rise to important consequences in their properties. Therefore, the study of the local structure of these compounds is of primary importance.

It is worth to mention here that many interesting literature papers on spinel ferrites which are dealing with the determination of cations in both lattice sites (A) and [B]. For instance, Dalet et al. [28] and Abbas et al. [29] reported that the distribution of cations in spinel ferrites is determined by the total energy of the lattice, whose parameter depends on some other factors, such as the size of ions (ionic radius), coulomb interactions between charges of these ions and the limited space between the repulsive forces, effects of polarization, and ordering of cations. Depending upon the nature (magnetic and nonmagnetic) as well as the distribution of cations among sub-lattices, spinel ferrites may exhibit different magnetic properties such as ferri-, antiferri-, ferro-, and antiferromagnetic. Moreover, Sepelak and Becker [30] confirmed and supported also this fact. They also reported that the cation distribution in spinel ferrites upon which many physical and chemical properties depend is in fact a complex function of processing parameters. For example, some spinel systems exhibit a temperature-dependent of cation distribution. This is in particular the case when there is only a slight difference between the lattice energies of the possible configurations. The structure will essentially be normal if the metal ions Me^{2+} occupy only tetrahedral sites then $x = 0$. If they occupy only octahedral sites, then the structure will become inverse ferrite, i.e., $x = 1$ at low temperatures, depending

on the configuration with lowest energy, and the cations tend to randomize among (A) and [B] sites with increasing temperature (the value of $x = 2/3$ corresponds to the completely random distribution of cations with maximum configurationally entropy). A rapid cooling of a spinel can quench in the high-temperature states. Thus, if the cation reordering is slow, the high-temperature disordering of cations may be preserved at lower temperature.

Studies dealing with pressure-induced structural transformations in spinels have shown that in addition to the temperature, an applied high pressure also may lead to a change in cation distribution. A spinel at high pressures exhibits a considerable degree of cation disordering in the anion framework. The pressure-induced disordering of cations may be preserved upon abrupt release of pressure, i.e., the recovered spinel may exhibit cation rearrangements, which is different from that in the initial untreated state. Similarly, irradiation of spinel with high-energy electrons, ions or neutrons, and gamma rays as well tends to randomize cation distribution on (A) and [B] lattice sites.

Naik et al. [31] noticed that high gamma radiations are known to produce irreversible changes in structural parameters and cation distribution which in turn induce modifications in electrical and magnetic properties of the material exposed to the radiation. These changes are a quantitative function of dose absorbed or given to the material. They were notified that ^{57}Fe Mössbauer spectroscopy as a nuclear probe technique for solid-state applications (e.g., electronic structures, bond properties, and magnetism) is very suitable for the investigation of the magnetic state, local symmetry, and charge states of Fe ions in iron containing substances among the spinel ferrites. The authors investigated structural, physical, and magnetic properties of gamma-irradiated $Mn_xZn_{1-x}Fe_2O_4$ nanoparticles using Mössbauer spectroscopy. Reduction of lattice constant, decrease in particle size, and increase in X-ray density were observed as direct consequences of gamma exposure. It was concluded also that cation distribution is greatly affected by gamma irradiation where Fe concentration in tetrahedral A site in gamma-irradiated samples is higher than Fe concentration at tetrahedral site in as-prepared samples. The observed increase in saturation magnetization after gamma irradiation is attributed to the rearrangement of cations at tetrahedral (A) and octahedral [B] sites in the lattice.

Deraz et al. [32] announced further that the distribution of cations depends on the method of preparation of spinel ferrites as well as the processing parameters therein such as the thermal history of the sample and the composition. The authors were interested to find out the cation arrangements of $CuFe_2O_4$ through the formula: $(Fe_{1-x}Cu_x)_A[Cu_{1-x}Fe_{1+x}]_BO_4$. The parameter of inversion x is equal to 0 for inverse spinel and to 1 when the spinel is normal. Cu^{2+} cations can be migrated from octahedral (B sub-lattice) to tetrahedral places (A sub-lattice). When the spinel is synthesized using classical ceramics technology (high-temperature treatment of initial oxides of the metal cations) with strict stoichiometry ($x = 1$), it has a tetragonal structure of hausmannite type. A number of methods have been devoted to study cation distribution, namely, Bertuat, Furuhashi Monte Carlo, and R-factor methods. R-factor method has been used by Rana et al. [33] for the determination of cation distribution in $Cu_{1-x}Zn_xFe_2O_4$ ferrites prepared by standard solid-state

Table 1 Inversion parameter (α), oxygen positional parameter (u), residual function (R) for $Cu_{1-x}Zn_xFe_2O_4$ ferrites [33]

Concentration (*x*)	(α)	(u)	(R)
0	0.25	0.32	0.03
0.25	0.2	0.32	0.09
0.5	0.2	0.32	0.09
0.75	0.2	0.32	0.07
1	0.2	0.32	0.04

reaction technique. The cation distribution in the studied samples was calculated using a computer program developed on the basis of R-factor method. In this method, the best structure is selected so that the value of residual function R is minimized. Several expressions for the residual function, R, are proposed, and two of these are:

$$R_1 = \frac{\sum_{hkl}\left|I_{obs}^{hkl} - I_{cal}^{hkl}\right|}{\sum_{hkl} I_{obs}^{hkl}} \text{ and } R_2 = \frac{\sum_{hkl}\left|\sqrt{I_{obs}^{hkl}} - \sqrt{I_{cal}^{hkl}}\right|}{\sum_{hkl}\sqrt{I_{obs}^{hkl.}}}$$

where I_{obs}^{hkl} and I_{cal}^{hkl} are the observed and calculated intensities for hkl reflections. The program was run for 10–100 iterations until the minimum value of the residual function R was obtained. The inversion parameter (α), oxygen positional parameter (u), and residual factors for each concentration of CuZn ferrites were calculated. The values of these three parameters are listed in Table 1, and cation distribution for $Cu_{1-x}Zn_xFe_2O_4$ ferrites is presented in Table 2.

Based on the data obtained from Table 2, they reported that Zn ions which have the strong preference for tetrahedral (A) site substituted for Cu ions having strong preference for octahedral [B] site, more and more Fe^{3+} ions will start migrating from (A) to [B], which results in an increase of magnetization of [B] site and reduction in magnetization of (A) site. This reduces the B-B interactions, and the A-B interaction starts increasing up to 50% contents of zinc because of the antiparallel arrangement of magnetic moments of (A) and [B] sites. With further substitution, a normal spinel $ZnFe_2O_4$ would be produced, but above 75% maximum anti-parallelism, the diminishing number of Fe_A ions and the Fe_B ions cannot be maintained against the increasing antiparallel interaction with B-ions lattice.

Heiba et al. [34] pointed out that huge number of publications addressed to the substitutions of nonmagnetic ions at Fe sites in Cu and/or Ni ferrite systems, viz., $NiFe_{2-x}Cd_xO_4$ and $NiAl_xFe_{2-x}O_4$. Most of these results confirmed that the cation distribution among (A) and [B] lattice sites depends on material's preparation. Lakhani et al. [35] studied the compositional dependence of structure parameters and X-ray Debye temperature for $CuAl_xFe_{2-x}O_4$, $0 \leq x \leq 0.6$ using the Rietveld analysis. Precise knowledge of the cation distribution over the crystallographic sites in magnetic oxides is crucial for understanding their physical properties.

Table 2 Cation distribution in $Cu_{1-x}Zn_xFe_2O_4$ ferrites [33]

	Tetrahedral (A)			Octahedral [B]		
Concentration (x)	Cu^{2+}	Zn^{2+}	Fe^{3+}	Cu^{2+}	Zn^{2+}	Fe^{3+}
Cation distribution						
0	0.25	0	0.75	0.75	0	1.25
0.25	0.15	0.2	0.65	0.6	0.05	1.35
0.5	0.10	0.4	0.5	0.4	0.1	1.5
0.75	0.05	0.6	0.35	0.2	0.15	1.65
1	0	1	0	0	0	2

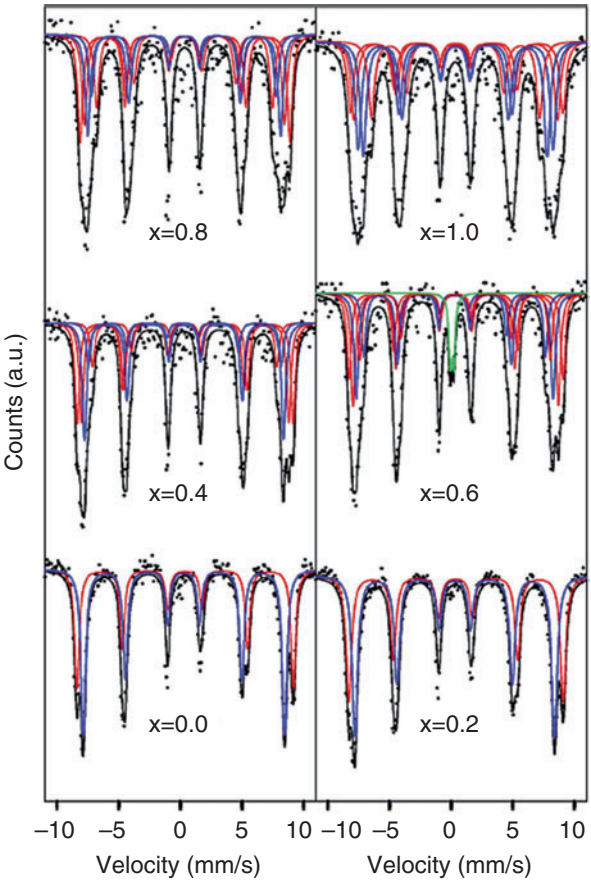

Fig. 2 Mössbauer spectra of nanocrystalline $NiFe_{1-x}Ga_xO_4$ ferrites, $0 \leq x \leq 0.1$ taken at 20 K (Reprinted from [36], Copyright (2014), with permission from Elsevier)

The details on how to use Mössbauer spectroscopy to find out the cation distribution are given below for two recent contributions that have been carried out by the author and his co-workers. For instance, Heiba et al. [36] studied the cation distribution and the dielectric properties of $NiFe_{1-x}Ga_xO_4$ ferrites, $0 \leq x \leq 1$. The system was prepared by citrate method in order to adopt the type of cation distribution by means

Table 3 Mössbauer hyperfine parameters at 20 K for $NiFe_{2-x}Ga_xO_4$ $0 \leq x \leq 1$ [36]

x	δFe (mm/s)	Δ(mm/s)	Hef (T)	A(%)	Site
0.0	0.27	0.02	50.7	0.42	A
	0.38	0.03	54.5	0.58	B
0.2	0.29	0.00	50.3	0.44	A
	0.37	0.04	54.0	0.56	B
0.4	0.25	0.08	50.5	0.25	A_0
	0.27	0.10	46.5	0.11	A_1
	0.36	0.04	54.5	0.24	B_0
	0.37	0.03	52.3	0.23	B_1
	0.36	−0.09	48.9	0.17	B_2
0.6	0.28	0.03	49.6	0.17	A_0
	0.26	0.06	45.7	0.25	A_1
	0.38	0.05	53.8	0.11	B_0
	0.37	0.02	51.7	0.24	B_1
	0.35	−0.06	48.0	0.23	B_2
	–	–	–	0.17	B_3
0.8	0.32	−0.02	48.6	0.23	A_0
	0.30	−0.07	46.6	0.14	A_1
	0.38	0.03	52.8	0.25	B_0
	0.31	0.05	50.4	0.21	B_1
	0.35	−0.03	44.3	0.17	B_2
1	0.36	0.01	49.1	0.24	A_0
	0.34	0.00	46.3	0.26	A_1
	0.41	0.07	53.6	0.16	B_0
	0.35	0.05	51.3	0.17	B_1
	0.34	0.03	42.3	0.17	B_2

of low-temperature Mössbauer spectroscopy. Figure 2 shows the Mössbauer spectra of $NiFe_{1-x}Ga_xO_4$ ferrite samples measured at 20 K. A summary of the hyperfine interaction parameters is given in Table 3. The Mössbauer spectrum of $NiFe_2O_4$ ($x = 0$) was fitted by two superimposed sextets ascribing the tetrahedral (A) and octahedral [B] sites. This result confirms the ferromagnetic nature of the compound $NiFe_2O_4$ [36]. It is well known also that $NiFe_2O_4$ has an inverse structure type, i.e., Fe^{3+} ions are equally distributed between tetrahedral (A) and octahedral [B] sites as $(Fe^{3+})_{tet}[Ni^{2+},Fe^{3+}]_{oct}O_4$. The spectra for $x \geq 0.4$ was fitted with five sextets, two assigned for (A) and three for [B] sites in consistent with the Yafet-Kittel model developed based on the extended Neel's model. It was shown that (A) and [B] sub-lattices may be subdivided into sub-lattices in such a way that the vector resultant of the magnetic moments of the sub-lattices are aligned in such directions that will influence the effective magnetism. On the other hand, introducing Ga^{3+} to replace Fe^{3+} will change the cationic distribution between (A) and [B] sites. Consequently, precise estimation of the cation distribution in $NiFe_{1-x}Ga_xO_4$ samples is crucial for understanding their physical (electric or magnetic) properties. In principle, the

Table 4 Refined values of cation occupancies (corresponding to inversion parameter λ) obtained from Rietveld refinements of $NiFe_{2-x}Ga_xO_4$ $0 \leq x \leq 1$ [36]

x	0.0	0.2	0.4	0.6	0.8	1.0
Occupancy factor						
C_A	Ni	0.16	0.24(1)	0.49(3)	0.34(5)	0.49(4)
	Fe	0.84	0.59	0.18	0.50	0.44
	Ga	0.0	0.17(1)	0.33(3)	0.16(5)	0.07(4)
C_B	Ni	0.84	1.21	0.51(3)	0.66(5)	0.51(4)
	Fe	1.16	0.03(1)	1.42	0.90	0.76
	Ga	0.0	0.76	0.07(3)	0.44(5)	0.73(4)
λ estimated from MS		0.84	0.76	0.51	0.66	0.51

inversion parameter varies based on five factors: (i) temperature, (ii) the electrostatic contribution to the lattice energy, (iii) cationic radii, (iv) cationic charge, and (v) crystal field effects. Since X-ray diffraction is unable to distinguish between the atoms closed together in periodic table, like Ga and Fe, the values of Fe occupancies in both (A) and [B] sites obtained from the Mössbauer data analysis (see Table 4) are used and fixed during Rietveld refinements. Additionally, the intensity of the peak relative area is able to provide information on cation distributions in $NiFe_{1-x}Ga_xO_4$ samples. The degree of cation inversion could be estimated from the line area ratio utilized during the fitting:

$$\frac{I_A}{I_B} = \frac{f_A}{f_B} \cdot \frac{y}{2-y} \tag{1}$$

where I_A and I_B represent the intensity between (A) and [B] sites, respectively, and y is inversion parameter. Ratio of the fractions (f_A/f_B) is equivalent to 0.94 at room temperature and 1 at low temperatures. Table 4 shows the Mössbauer estimation of the ionic distribution in $NiFe_{1-x}Ga_xO_4$ ferrite samples. It can be noticed that the inversion parameter deceases with the increase of Ga content, indicating partial inversion and the system at $x \geq 0.6$ is slowly transforms into a normal spinel.

Catalytic Activity of the Oxide Spinels (OSs)

Spinels as Catalysts for Soot Combustion

Diesel (DI) engines have become popular worldwide due to their higher thermal efficiency and lower fuel consumption than gasoline engines [37]. But diesel engine exhaust emissions consist of the products of combustion including particulate matter (soot), nitrogen, water, carbon monoxide, nitrogen and sulfur oxides, and polycyclic aromatic hydrocarbons (PAH). The conceptual model of DI combustion process and formation soot and NO_x are shown in Fig. 3.

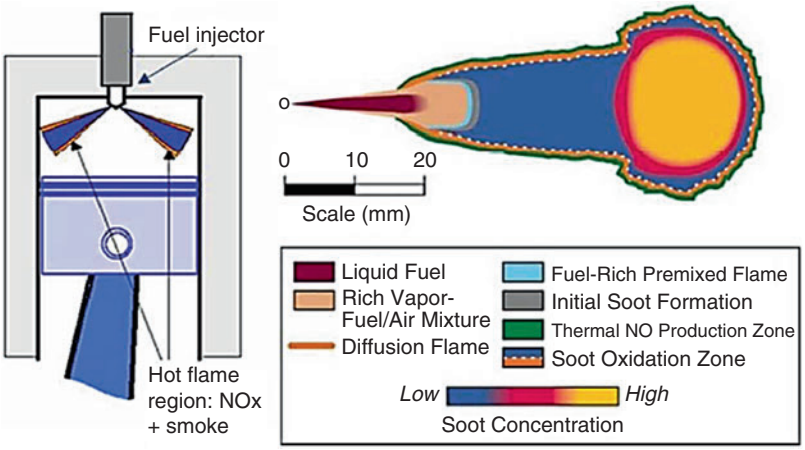

Fig. 3 Conceptual model of DI combustion process, soot, and NO_x formation (Reprinted from [37], Copyright (2017), with permission from Royal Society of Chemistry)

It is well known that soot particulate (mainly carbon nano-particulate) causes air pollution and is harmful for human health. Out of this, DPF (diesel particulate filter) is considered as the most popular and efficacious technology for soot elimination [38]. These filters usually consist of wall-flow monoliths with honeycomb-like structures with 50% of the channels plugged at the gas entry side and the remaining channels plugged at the exit. The gas stream enters into the filter through the open channels and is forced to pass through the porous walls where the soot particles get stuck. However, the accumulation of soot on the filter's wall will decrease the efficiency of DPF. Diesel particulate matter burns when temperatures above 600 °C are attained. This temperature can be reduced to the range 350–450 °C by using of a fuel catalyst.

Legutko et al. [39] have investigated how potassium (K) precursor nature and doping level change the catalyst activity of Mn and Fe spinels in the soon oxidation reaction. The catalysts were prepared by weighing 1 g of commercial spinel Mn_3O_4 and Fe_3O_4, 6 and 35 m^2/g, respectively, and then adding an appropriate amount of potassium precursor/salt (KOH, K_2CO_3, KNO_3, CH_3COOK, and K_2SO_4) solution to achieve the desired alkali loading: 0.2 and 1 wt.% for Mn_3O_4 and Fe_3O_4, respectively. For Fe_3O_4, it was found that alkali doping (0.5 monolayer) enhanced its catalytic activity ($\Delta T_{50\%} \approx 80$ °C for K_2CO_3). For Mn_3O_4 K-doping (9 ML), the formation of a birnessite (KMn_4O_8) phase on Mn_3O_4 core catalyst with a spectacular increase of the soot oxidation rate ($\Delta T_{50\%} \approx 150$ °C) was observed (Fig. 4a, b).

The same research group [40] has reported about the effect of alkali promotion of Fe_3O_4 catalyst in soot combustion. Iron-based catalysts have attracted considerable attention as soot combustion catalytic materials due to their low price and environmental friendliness. The concentration of alkali metals in the prepared catalysts varied in the range of 0.1–3.5 wt.%. It was found that the minimum of the work function, related to the optimum alkali loading, corresponds to the highest soot

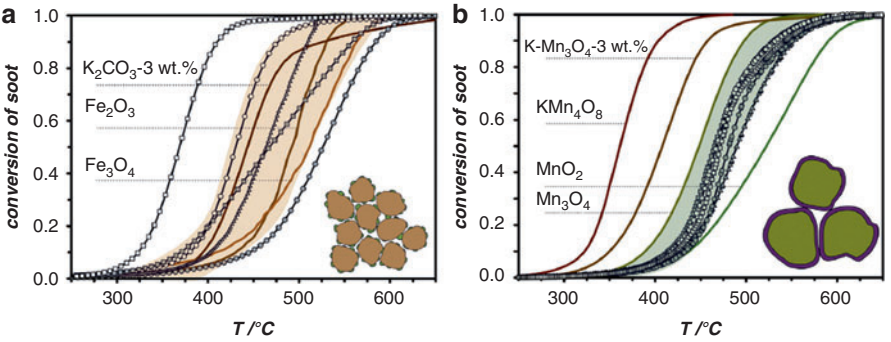

Fig. 4 Conversion of soot on K-doped iron (**a**) and manganese (**b**) spinels. Respective lines denote doping with different precursors: K_2CO_3, empty circles (○); KOH, filled triangles (▲); CH_3COOK, filled squares (■); KNO_3, empty squares (□); and K_2SO_4, filled circles (●) (Reprinted from [39], Copyright (2014), with permission from Elsevier)

combustion activity. The promotional effect increases in the sequence of the ionic radii of the alkali elements promoters: Li < Na < K < Cs. The Cs-doped Fe_3O_4 catalyst decreases the $T_{50\%}$ value from700°C for non-catalytic soot combustion to 390 °C (Fig. 5a).

Liu et al. [41] reported about highly efficient catalysts $Mn_{1-x}Ag_xCo_2O_4$ spinel oxide, prepared via sol-gel method. Soot in the non-catalytic combustion was not consumed completely until reaction temperature reached above 600 °C. $Mn_{0.6}Ag_{0.4}Co_2O_4$ catalyst displayed the highest catalytic activity for soot combustion among the five selected catalysts, and the lowest temperature of soot combustion, T_{10}, T_{50}, T_{90}, and T_m, is 250 °C, 325 °C, 373 °C, and 334 °C, respectively (Fig. 5a). The reason on the highest catalytic activity is a result of the synergetic effect of chemisorbed oxygen species (O^{2-}, O^-) and metallic silver.

Other different spinel oxides as noble metal-free compounds ($CoCr_2O_4$, $MnCr_2O_4$, $CoFe_2O_4$, Cu-doped $ZnAl_2O_4$, etc.) have been reported as promising candidate catalysts for diesel soot combustion, due to their good redox properties and thermochemical stability [42, 43].

Spinels as Catalysts for N_2O Decomposition

Nitrous oxide (N_2O) is a strong greenhouse gas with a global warming potential approximately 300 times higher than that of CO_2 and also contributes to the destruction of the stratospheric ozone layer [44]. **N_2O** has been identified as a contributor to the destruction of ozone in the stratosphere and recognized as a relatively strong greenhouse gas [45]. It is emitted during agricultural (land cultivation, biomass burning) and industrial activities (during the combustion of stationary and mobile fossil fuels and solid waste). The human activities, such as the production of adipic acid and nitric acid, are one of the main sources for N_2O production.

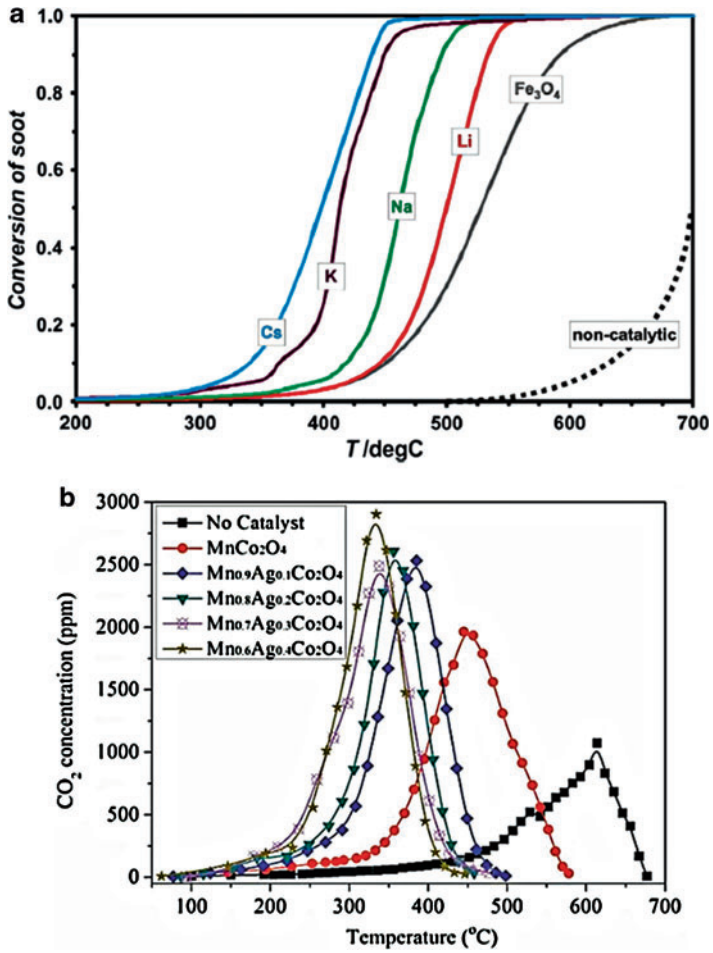

Fig. 5 (**a**) Soot conversion as a function of temperature for optimized alkali (Li-0.2 wt.%, Na-0.8 wt.%, K-1 wt.%, Cs-2 wt.%)-doped Fe_3O_4 and reference magnetite. Dotted line corresponds to the non-catalytic soot combustion (Reprinted from [40], Copyright (2014), with permission from Elsevier); (**b**) The CO_2 concentration curves for soot combustion over $Mn_{1-x}Ag_xCo_2O_4$ ($x = 0$, 0.1, 0.2, 0.3, 0.4) catalysts (Reprinted from [41], Copyright (2017), with permission from Elsevier)

N_2O molecule is quite stable at room temperature and has an estimated lifetime in the atmosphere of about 150 years [45]. Many researchers make their efforts to develop catalysts facilitating N_2O abatement and catalytic decomposition of N_2O into N_2 and O_2.

The reaction of N_2O decomposition can be described as an adsorption of N_2O at the catalyst's active centers, usually a transition metal ion, followed by a decomposition giving formation of N_2, and a surface oxygen. This surface oxygen can be desorbed by combination with another oxygen atom or by direct reaction with another N_2O [45]:

$$N_2O + *^{k1}{}_{k_1}\ N_2O^*$$

$$N_2O^*\ ^{k2}{}_{k_2}\ N_2 + O^*$$

$$2O^*\ ^{k3}{}_{k_3}\ O_2 + 2^*$$

$$N_2O + O^*\ ^{k4}{}_{k_4}\ N_2 + O_2 + *$$

The reaction of N_2O with the catalysts active centers is generally envisaged as a charge donation from the catalyst into the antibonding orbitals of N_2O, destabilizing the N-O bond and leading to its breaking [45].

Nowadays, many catalysts have been reported, including noble metals [46], pure and metal-doped oxides [47–50], mixed oxides [44, 51, 52], and zeolitic systems [53–55]. Among them, mixed oxide systems containing Co spinel showed the best catalytic activity in the decomposition of N_2O. The researcher's efforts are focused more on the development of more active and stable systems and also on the better understanding of catalytic mechanism over different catalytic systems.

Abu-Zied et al. [56] have performed direct catalytic decomposition of N_2O into N_2 and O_2 over $Cu_xCo_{1-x}Co_2O_4$ ($x = 0.0 \leq x \leq 1.0$) spinel oxide catalysts synthesized by the co-precipitation method followed by calcination at 500 °C. The catalytic performance was evaluated in an isothermally operated plug-flow reactor. It appeared that the spinel oxides containing Cu and Co are more active than the individual oxides, i.e., CuO and Co_3O_4. It was shown that the presence of Cu ions enhances the thermal reduction of Co^{3+} ions, which lead to a weakening of the N-O bond and increasing the N_2O decomposition activity. The $Cu_{0.75}Co_{0.25}Co_2O_4$ catalyst shows higher N_2O decomposition activity than that of the other catalysts in this series: 100% decomposition at 500 °C (conditions: 500 ppm N_2O in N_2; total flow, 200 $cm^3\ min^{-1}$; and weight of catalyst, 0.5 g).

Various spinel-type catalysts AB_2O_4 (where A = Mg, Ca, Mn, Co, Ni, Cu, Cr, Fe, Zn and B = Cr, Fe, Co) were prepared by solution combustion method by Russo et al. [57]. Spinel-type oxides containing Co at (B) site were found to provide the best activity. The half conversion temperature of N_2O over $MgCo_2O_4$ catalyst was 440 °C and 470 °C in the absence and presence of oxygen, respectively (GHSV = 80,000 h^{-1}), due to its greater capability to form surface vacancies, which was pointed out as the key player in N_2O catalytic decomposition.

Partial substitution of the A- and B-cations by other divalent 3D transition metals (Mg, Cr, Mn, Ni, Cu, Zn, etc.) creates special chemicophysical properties of spinels, changes their inversion degree, and makes them attractive for catalytic applications. For example, Yan et al. [58] investigated such substitution. The catalytic decomposition of N_2O to N_2 and O_2 has been proposed for $M_xCo_{1-x}Co_2O_4$ (M = Ni^{2+} and Mg^{2+}, $x = 0.0$–0.99) spinel catalysts, prepared by co-precipitation method. The conversion of N_2O reached 100% over the $Ni_{0.74}Co_{0.26}Co_2O_4$ and $Mg_{0.54}Co_{0.46}Co_2O_4$ catalysts at 200 °C and 300 °C in the absence and presence of excess O_2 and water steam, respectively.

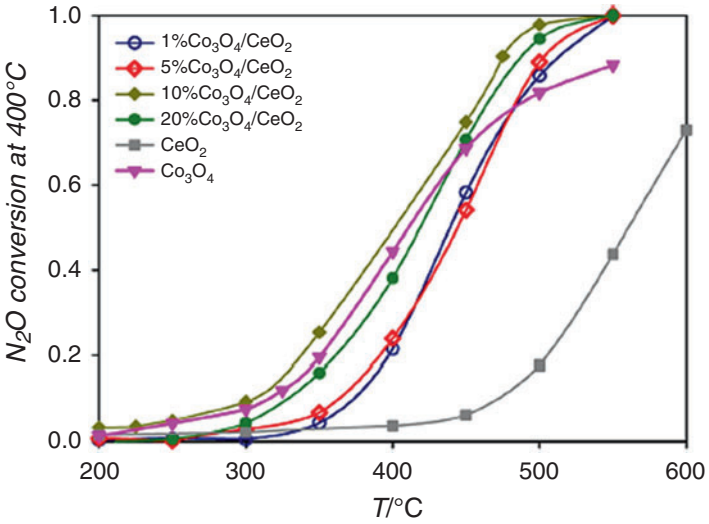

Fig. 6 Conversion curves for N_2O decomposition reaction over the Co_3O_4/CeO_2 catalysts (Reprinted from [59], Copyright (2016), with permission from Elsevier)

Supported oxides are important for practical applications due to their higher dispersion by combination with the larger specific surface area of the support. A supported Co_3O_4/CeO_2 catalyst has been investigated by Grzybek et al. [59] for high deN_2O activity, in order to understand the mechanistic role of active phase/support periphery. A series of Co_3O_4/CeO_2 catalysts with increasing cobalt spinel loading in the range of 1–20 wt.% was prepared by incipient wetness impregnation of CeO_2. The catalytic tests in deN_2O reaction revealed that the 10 wt.% of Co_3O_4 in supported system is able to reproduce the activity of bare Co_3O_4 catalyst. However, it was found that the catalyst with the lowest content of Co_3O_4 equal to 1 wt.% exhibits the highest apparent reaction rate per mass of the spinel active phase (Fig. 6).

Another supported catalytic system has been reported by Grzybek et al. [60]. A series of monolithic catalysts with 0.3 wt.% loading of (Co,Zn)Co_2O_4 spinel active phase dispersed on bare and ceria and zincite washcoated cordierite substrates were prepared by impregnation method: (Co,Zn)Co_2O_4/cordierite, (Co,Zn)Co_2O_4/ZnO/cordierite, and (Co,Zn)Co_2O_4/CeO_2/cordierite (Fig. 7). The catalytic deN_2O activity of catalysts was investigated using model gas mixture (2000 ppm N_2O/N_2) and tail gases (1400 ± 50 ppm N_2O, 900 ± 100 ppm NO_x, 0.8 ± 0.2 vol.% H_2O, 2.0 ± 0.2 vol.% O_2) of the nitric acid pilot plant. The catalytic tests revealed that the monolithic catalysts exhibit high catalytic deN_2O activity, reaching $X > 96\%$ at 400 °C (model gas) and 450 °C (tail gases) for the best (Co,Zn)Co_2O_4/CeO_2/cordierite system (Fig. 8). It was also found that the specific reaction rate per Co_3O_4 weight loading for the monolithic catalysts is even two orders of magnitude higher than in the case of the optimized bulk spinel phase.

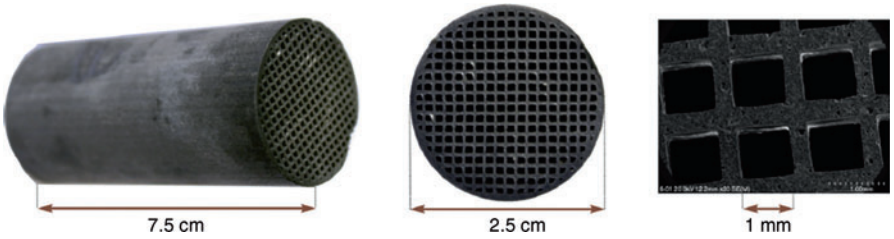

Fig. 7 The representative images of monolithic system: (Co,Zn)Co_2O_4/CeO_2/cordierite (Reprinted from [60], Copyright (2015), with permission from Elsevier)

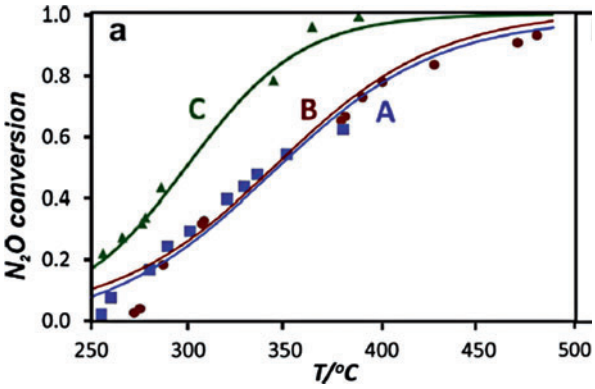

Fig. 8 Comparison of the deN_2O activity of the monolithic catalysts (**a**) (Co,Zn)Co_2O_4/cordierite, (**b**) (Co,Zn)Co_2O_4/ZnO/cordierite, and (**c**) (Co,Zn)Co_2O_4/CeO_2/cordierite in model gas mixture (2000 ppm N_2O/N_2, V = 0.5 L/min) (Reprinted from [60], Copyright (2015), with permission from Elsevier)

Spinels as Catalysts for CO Oxidation

Carbon monoxide (CO) is a detrimental air pollutant that gives rise to harmful health and environmental effects. It not only affects human beings but also vegetation and indirectly increases global warming. It is a toxic gas that can effectively convert a large fraction of hemoglobin in human blood to carboxyhemoglobin if the level in atmosphere is around 100 ppm. Exhaust gases are neutralized using catalysts based on platinum metals with low initial working temperatures (473–628 K). However, the high cost of noble metal catalysts imposes the need for developing other catalytic systems that do not contain platinum family metals. During recent years, research has been carried out on mixed oxides of transition metals, of the type $A^{II}B^{III}{}_2O_4$ with spinel structure, which are active, thermally stable, and more resistant toward catalyst poisoning [61, 62]. Among them are Co_3O_4 [63], Co_3O_4/TiO_2 [64], $CuFe_2O_4$ [65], $CuCr_2O_4$ [66, 67], CoAlFe nonstoichiometric spinel-type oxides [68], etc. It was shown that Co_3O_4 with a spinel structure containing Co^{3+} in an octahedral coordination and Co^{2+} in tetrahedral coordination is a very active oxide catalyst for the oxidation of CO.

The series of CoAlFe mixed oxides with nonstoichiometric spinel structure derived from hydrotalcites were prepared by Lv et al. [68]. Compared with the binary oxides and Co_3O_4, Co-Al-Fe ternary oxides displayed much larger catalytic

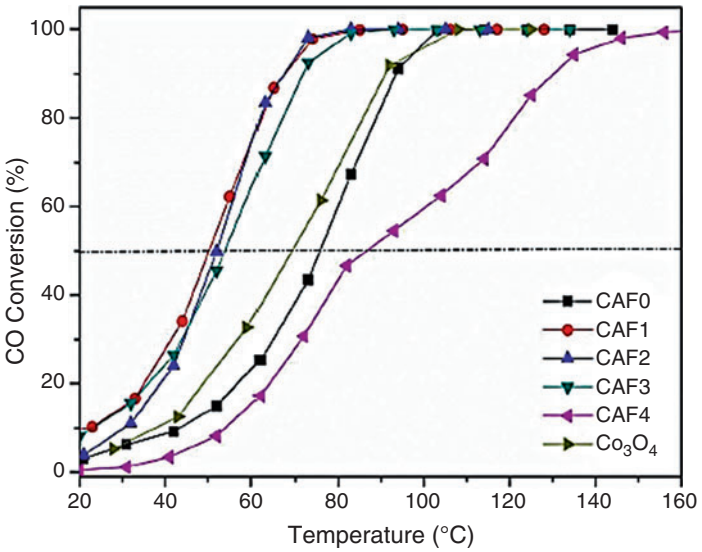

Fig. 9 Efficiency of the catalytic oxidation of CO over CoAlFe-500 (Reprinted from [68], Copyright (2016), with permission from Royal Society of Chemistry)

activity for CO oxidation with complete CO conversion at 80 °C (Fig. 9). The effect of Fe doping into the cobalt-based spinels improved low-temperature reducibility due to the enhanced surface area. It was proved that according to the in situ FTIR analysis, CO adsorbed on the catalyst surface reacted with surface lattice oxygen to form CO_2.

Cu-Cr mixed oxides catalysts with various Cu-Cr molar ratios were prepared using the hydrothermal method by Mobini et al. [66]. The activity of the catalysts was measured in the temperature range of 50–400 °C on the CO oxidation reaction. For catalyst with ratio Cu:Cr = 1:2 ($CuCr_2O_4$), the smallest particle size (22 nm) and the highest surface area (46.9 m^2/g) were observed. It was confirmed that $CuCr_2O_4$ spinel phase has higher activity than CuO phase for CO oxidation due to the fact that $CuCr_2O_4$ spinel phase can generate surface oxygen easier than CuO or Cu on the surface and the reaction is more progressed over $CuCr_2O_4$ phase. For CO oxidation at 250 °C, the Cu/Cr = 1:2 sample showed that the highest CO reaction rate of $72.6 \cdot 10^{-6}$ mol/(g.s) and CO oxidation activity ($T_{50\%}$ and $T_{90\%}$) were calculated as 110 and 114 °C, respectively, (Fig. 10a).

Mobini et al. [67] have reported about $CuCr_2O_4$ catalysts synthesized by hydrothermal method with the use of cetyltrimethyl ammonium bromide (CTAB) as surfactant. The samples were annealed at different temperatures (160, 180, and 200 °C) for 11 h, and the resulting precipitate was calcined at various temperatures (400, 500, 600, and 700 °C) for 4 h. The $CuCr_2O_4$ prepared under a hydrothermal temperature of 180 °C possessed the highest specific surface area and better catalytic performance. The increase in calcination temperature from 400 °C to 700 °C led to an important decrease in BET area from 54.6 to 16.7 $m^2\ g^{-1}$ and an increase in

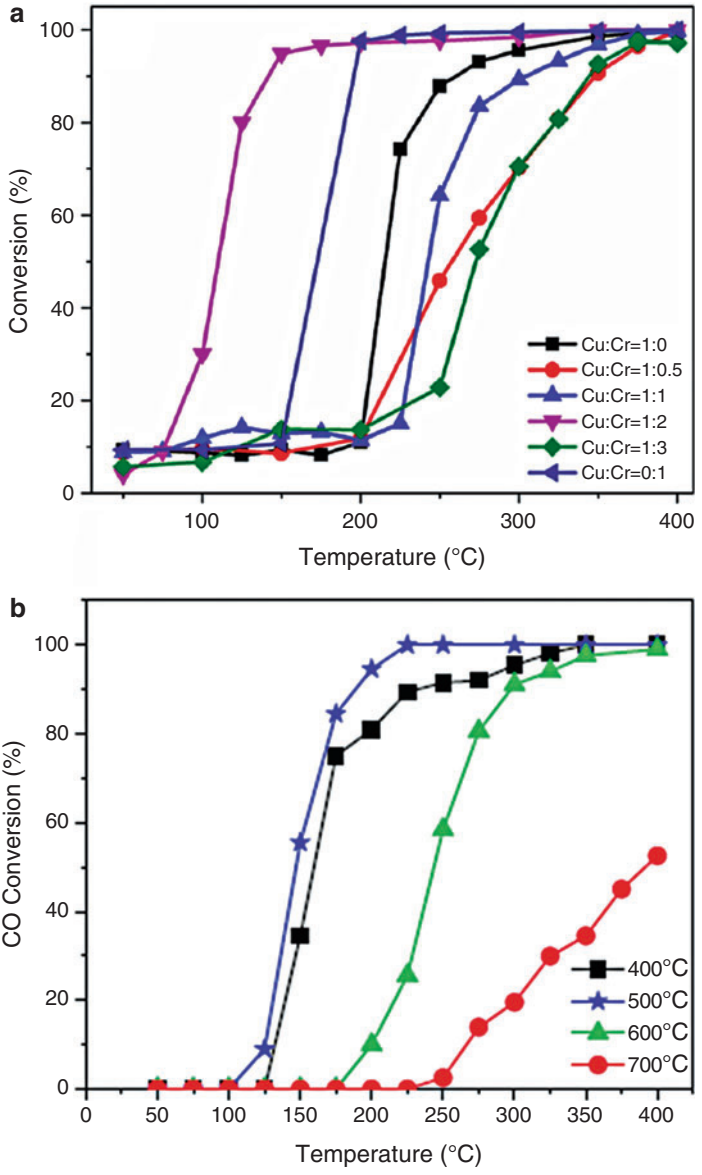

Fig. 10 (**a**) CO conversion as a function of reaction temperature over the nanocrystalline copper-chromium catalyst (reaction conditions: 10% CO and 20% O_2 balanced with Ar, GHSV = 60,000 ml/g.h, pretreated in oxidative atmosphere) (Reprinted from [66], Copyright (2017), with permission from Elsevier); (**b**) CO conversion of the $CuCr_2O_4$ catalysts prepared under different calcination temperatures. Preparation conditions, pH = 12, aging time = 4 h, and autoclave temperature = 180 °C for 11 h; reaction conditions, GHSV = 60,000 mL/h.gcat and CO/O_2 feed ratio = 0.1 (Reprinted from [67], Copyright (2017), with permission from Elsevier)

crystal size from 7.9 to 23.9 nm (Fig. 10b). The best catalytic performance was obtained for the sample calcined at 500 °C, which had both appropriate crystalline phase and high surface area.

The catalytic activity of Zn-substituted lithium ferrites $Zn_yLi_{0.5-0.5y}Fe_{2.5-0.5y}O_4$ (where $0.0 \leq y \leq 1.0$ with step 0.1) in the CO oxidation was investigated by Tatarchuk [62] and the new antistructural modeling was proposed for the catalysis explanation. According to the antistructural model [69], the interaction of CO with oxygen on the surface of a ferrite-containing catalyst was studied. The first step in the process is the adsorption of gaseous O_2 and CO on the surface active centers Li_B'' and $Fe_A^{\bullet}$, respectively, in the lithium ferrite case:

$$(1-\alpha)Fe_A^{\bullet}\left[Li_{0,5}''Fe_{1,5}^{\times}\right]_B\left(O_4^{\times}\right)_O + 2\alpha O_2 + \alpha V_A''\left[V_2'''\right]_B\left(V_4^{\bullet\bullet}\right)_O \rightarrow$$
$$\rightarrow \left(Fe_{1-\alpha}^{\bullet}V_{\alpha}''\right)_A\left[Li_{0,5-0,5\alpha}''Fe_{1,5-1,5\alpha}^{\times}V_{2\alpha}'''\right]_B\left(O_4^{\times}\right)_O + 8\alpha h^{\bullet}$$

$$Fe_A^{\bullet}\left[Li_{0,5}''Fe_{1,5}^{\times}\right]_B\left(O_4^{\times}\right)_O + 4\alpha CO \rightarrow Fe_A^{\bullet}\left[Li_{0,5}''Fe_{1,5}^{\times}\right]_B\left(O_{4-4\alpha}^{\times}V_{4\alpha}^{\bullet\bullet}\right)_O + 4\alpha CO_2 + 8\alpha e'$$

A combination of this both reactions favors the route of CO oxidation over ferrite-containing catalyst, and the catalyst returned to its initial state:

$$\left(Fe_{1-\alpha}^{\bullet}V_{\alpha}''\right)_A\left[Li_{0,5-0,5\alpha}''Fe_{1,5-1,5\alpha}^{\times}V_{2\alpha}'''\right]_B\left(O_4^{\times}\right)_O + Fe_A^{\bullet}\left[Li_{0,5}''Fe_{1,5}^{\times}\right]_B\left(O_{4-4\alpha}^{\times}V_{4\alpha}^{\bullet\bullet}\right)_O + 2\alpha O_2 + 4\alpha CO \rightarrow$$
$$\rightarrow (2-\alpha)Fe_A^{\bullet}\left[Li_{0,5}''Fe_{1,5}^{\times}\right]_B\left(O_4^{\times}\right)_O + 4\alpha CO_2 + \underbrace{\alpha V_A''\left[V_2'''\right]_B\left(V_4^{\bullet\bullet}\right)_O}_{\text{annigilation}} + \underbrace{8\alpha h^{\bullet} + 8\alpha e'}_{\text{annigilation}}$$

For zinc ferrite, the adsorption of gaseous O_2 and CO will be on the crystal lattice own defects (cationic and anionic vacancies), which acts as active centers:

$$\left(Zn_{1-\mu}V_{\mu}''\right)_A\left[Fe_{2-2\mu}^{\times}V_{2\mu}'''\right]_B\left(O_{4-8\mu}^{\times}V_{8\mu}^{\bullet\bullet}\right)_O + 2\mu O_2 + 4\mu CO \rightarrow$$
$$\rightarrow (2-2\mu)Zn_A^{\times}\left[Fe_2^{\times}\right]_B\left(O_4^{\times}\right)_O + 4\mu CO_2 + \underbrace{2\mu V_A''\left[V_2'''\right]_B\left(V_4^{\bullet\bullet}\right)_O}_{\text{annigilation}} + \underbrace{8\mu h^{\bullet} + 8\mu e'}_{\text{annigilation}}$$

Catalytic Activities OS in the Other Processes

Heterogeneous catalytic hydrogenation of gaseous **carbon dioxide** (CO_2) **to methanol** (CH_3OH) was investigated by Matej Huš et al. [70] on $Cu/ZnAl_2O_4$ spinel-type heterogeneous catalysts. The density functional theory (DFT) calculations were carried out to assess the thermodynamics and to elucidate the pathway leading to the formation of methanol from CO_2 on realistic spinel-type trimetallic material $Cu/ZnAl_2O_4$. The catalyst $Cu/ZnO/Al_2O_3$ was synthesized via co-precipitation at a constant pH (~8) and a constant temperature (60 °C). The catalyst was modeled as $ZnAl_2O_4$ in a spinel structure with active cluster Cu_3Zn_3 on its (110) plane, deposited

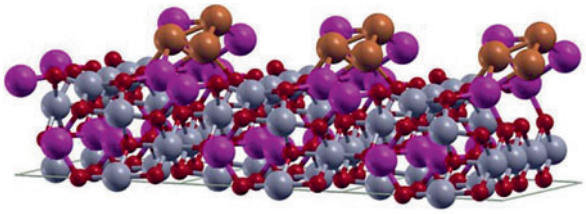

Fig. 11 Active cluster Cu_3Zn_3 on top of 110 plane of $ZnAl_2O_4$ support. Left, three unit cells in perspective; right, top view of a single unit cell. Cu atoms are shown in bronze, Zn in purple, Al in gray, and O in red (Reprinted from [70], Copyright (2017), with permission from Elsevier)

in the most favorable position (Fig. 11). The results demonstrate that Cu and Zn synergy is crucial for CO_2 hydrogenation to CH_3OH, which is proposed to form through HCOO, H_2COO, H_2COOH, CH_2O, and CH_3O species.

Ghosh et al. [71] have designed a catalyst composed of CuO, mesoporous TiO_2, and $CoFe_2O_4$ nanoparticles and investigated its catalytic activity toward **reduction of 4-nitrophenol** and a herbicide "trifluralin" in the presence of excess of $NaBH_4$. The novel nanocatalyst offered easy magnetic separation after the catalysis reaction and excellent reusability. It was observed that the time required for complete reduction of 4-NP was only 5 min (Fig. 12a) and the rate of the reaction was 0.72 min^{-1}. The catalytic reduction reaction occurred via relaying of electrons from BH_4^- donor to the acceptor 4-NP. The catalyst can also be reused for several times without any significant decrease of its activity (Fig. 12b).

Zinc aluminate spinel ($ZnAl_2O_4$) is widely used in many catalytic applications including cracking, dehydration of saturated alcohols, synthesis of methanol, and other alcohols in addition to acting as a support for catalysis. Sr-doped $ZnAl_2O_4$ nanomaterials with spinel structure were prepared by Kumar et al. [72] through modified sol-gel method using ethylenediamine followed by sintering at 900 °C. Higher activity was obtained for the conversion of benzyl alcohol to benzaldehyde for 0.3 molar percentage Sr(II)-added zinc aluminate in the presence of H_2O_2 as oxidant in acetonitrile medium. Among the prepared nanomaterials, the sample with molar ratio of Zn:Sr:Al = 0.7:0.3:2 is found to have 99% selectivity toward the oxidation of all the alcohols (butanol, hexanol, heptanol, octanol, cyclohexanol, 1-phenyl ethanol, and 4-methyl benzyl alcohol) in the [72].

$CuAl_2O_4$ spinel prepared by modified sol-gel technique as catalyst for the oxidation of benzyl alcohol to benzaldehyde has been reported by Kumar et al. [73]. The addition of ethylenediamine during the preparation procedure enhances its catalytic properties: the conversion of benzyl alcohol reaches a maximum 100% under the following reaction conditions: catalyst, 1 g; acetonitrile, 10 mmol; H_2O_2, 10 mmol; temperature, 80 °C; and time, 10 h.

Recently, it was found that cobalt salt could be used as catalysts in the hydrolysis of $NaBH_4$ to produce clean H_2 gas [74, 75]. Tomboc et al. [76] reported about spinel Co_3O_4 macrocube catalyst for H_2 generation from $NaBH_4$ (Fig. 13a). A high H_2 generation rate of 1497.55 mlH_2 min^{-1} $gcat^{-1}$ was obtained from the hydrolysis

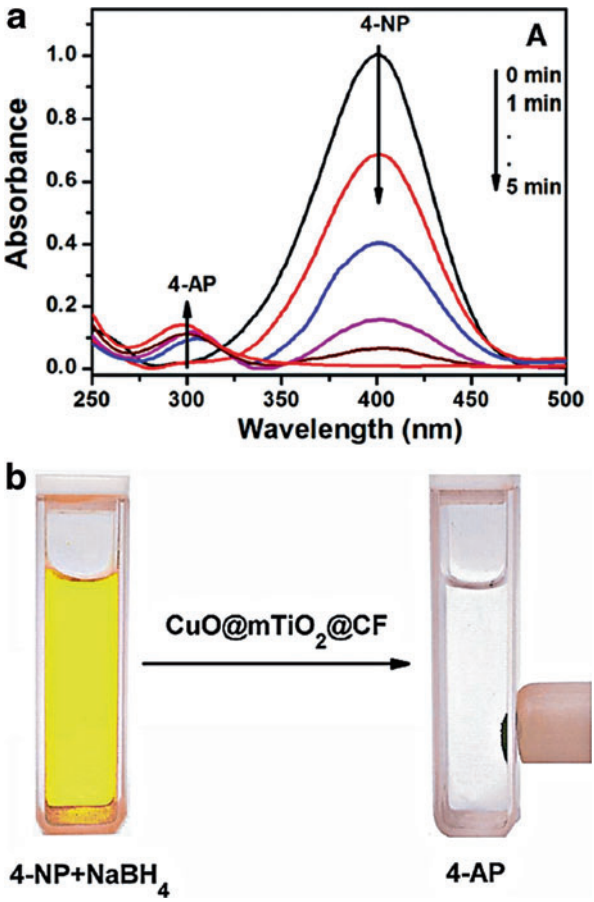

Fig. 12 (**a**) Time-dependent UV-vis spectral changes of the reaction mixtures of 4-NP and $NaBH_4$ catalyzed by $CuO@mTiO_2@CF$; (**b**) reduction of 4-NP in the presence of $NaBH_4$ and $CuO@mTiO_2@CF$ catalyst and magnetic separation of $CuO@mTiO_2@CF$ catalyst by applying a magnet externally after completion of reaction (Reprinted from [71], Copyright (2017), with permission from Springer)

of 2 wt % $NaBH_4$ solution with 0.02 g catalyst at 25 °C. This new Co_3O_4 macrocube catalyst was obtained by using a novel chitosan/urea template and exhibited super catalytic activity toward the hydrolysis of alkaline $NaBH_4$ solution for H_2 generation and shown stable activity during five cycles (Fig. 13b).

The catalytic activity of ferrites can be evaluated in the **fabrication of carbon nanotubes (CNTs)**. For example, Akbarnejad et al. [77] investigated the catalytic activity of some spinel ferrite nanocrystal Ni/Co ferrites ($Ni_xCo_{1-x}Fe_2O_4$ with $x = 0$, 0.2, 0.4, 0.6), Ni/Zn ferrites ($Zn_yNi_{1-y}Fe_2O_4$ with $y = 0.3$, 0.5, 0.7, 1), and copper ferrite ($CuFe_2O_4$) on the growth of CNTs. The CNTs were grown by the catalytic chemical vapor deposition (CVD) method from acetylene (C_2H_2) as carbon source and with using of 0.05 g of catalyst. The growth temperatures were selected equal to the calcination temperatures. It was found that the catalytic activity is higher for $Ni_{0.6}Co_{0.4}Fe_2O_4$ sample among the Ni/Co ferrites and for $Zn_{0.5}Ni_{0.5}Fe_2O_4$ sample among the Ni/Zn ferrites due to higher catalytic activity of Ni compared to Co and Zn and due to the structural isotropy.

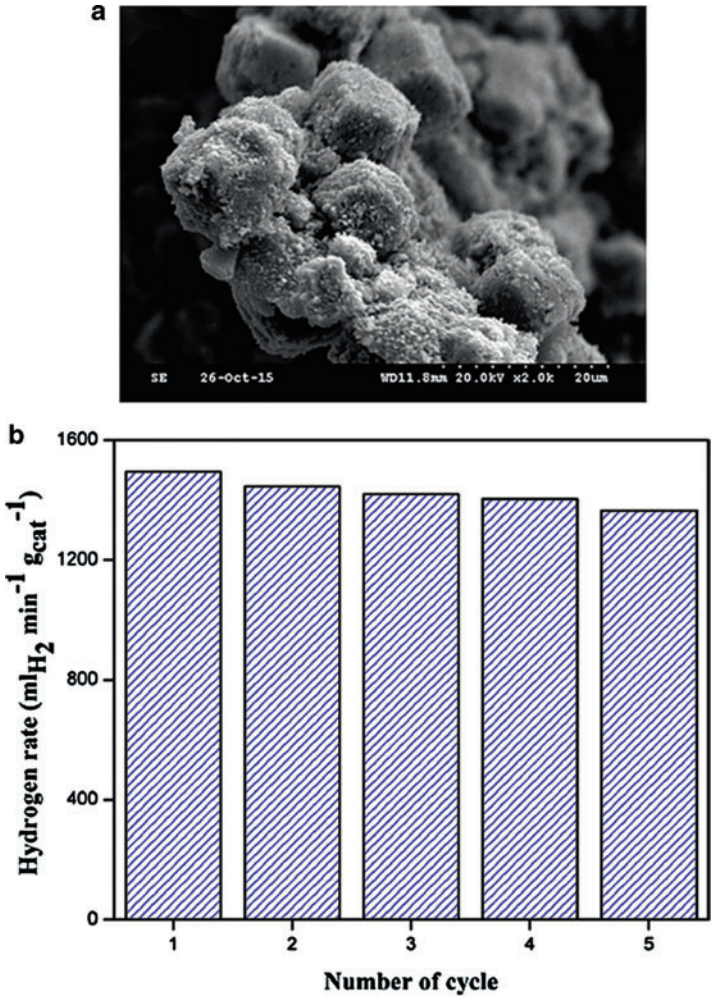

Fig. 13 Co_3O_4 macrocube catalyst: (**a**) SEM images of Co_3O_4 macrocube catalyst calcined at temperature: 700 C; (**b**) recycling performance of Co_3O_4 macrocube catalyst with chitosan/urea template (Reprinted from [76], Copyright (2017), with permission from Elsevier)

Zampiva et al. [78] reported about $MgFe_2O_4$ which has also been used as a catalyst in the production of carbon structures such as CNTs. The multi-walled carbon nanotubes (MWNTs) were synthesized by CVD using Mg ferrite as catalyst to produce 3D carbon macrostructures. $MgFe_2O_4$ obtained by sol-gel auto-combustion method with glycine as fuel and annealed at 1100 °C presented a distinct higher MWNT production compared to the other samples annealed at lower and higher temperatures. Raman spectra (Fig. 14a) reveal typical MWNT characteristics D, G, and G bands at 1342 cm^{-1}, 1572 cm^{-1}, and 2738 cm^{-1}, respectively [62, 63]. The MWNT quality and quantity are measured by the (I_D/I_G) ratio (Fig. 14a),

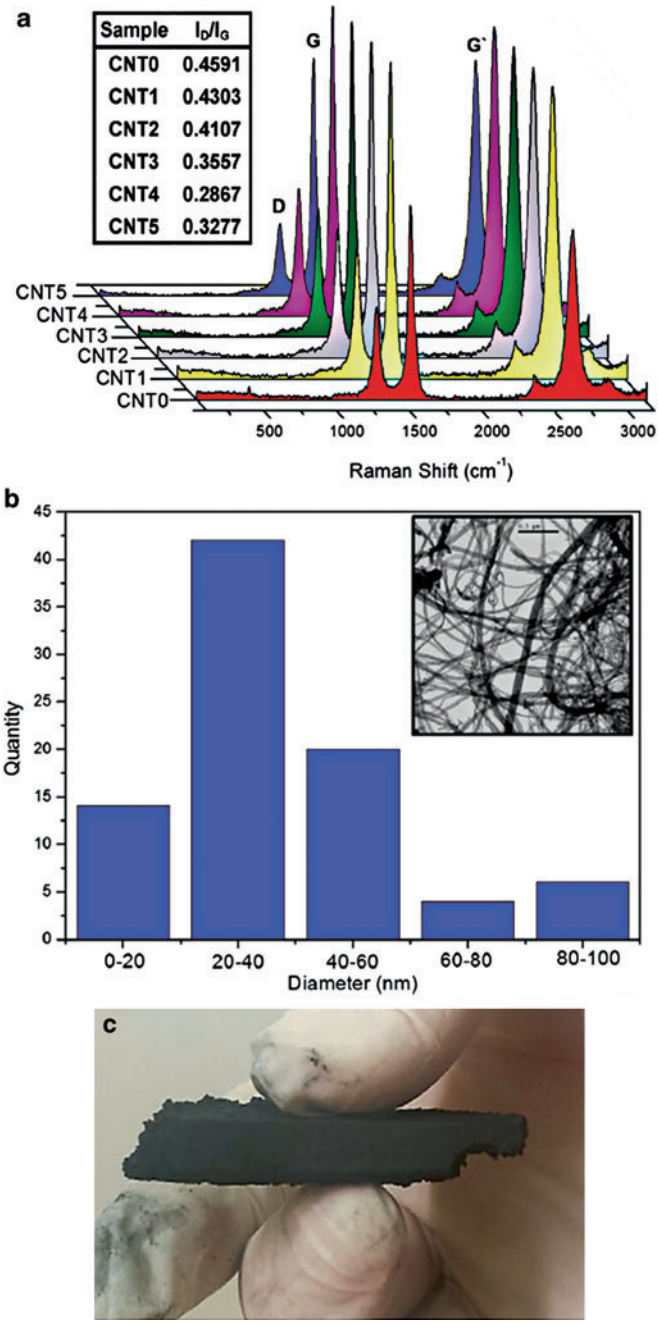

Fig. 14 3D CNT macrostructure synthesis catalyzed by $MgFe_2O_4$ nanoparticles: (**a**) Raman spectroscopy of the MWNT samples obtained with using $MgFe_2O_4$ as catalyst (CNT0 = as-prepared $MgFe_2O_4$; CNT1 = $MgFe_2O_4$ (500 °C); CNT2 = $MgFe_2O_4$ (700 °C); CNT3 = $MgFe_2O_4$ (900 °C);

while the G band specifies the MWNT purity degree. It was shown that only the CNT4 ($MgFe_2O_4$-1100 °C; with the highest graphitization degree) had sufficient production to generate a well-defined 3D macrostructure (Fig. 14b, c).

According to the generally accepted growth mechanism of CNTs, the CNT diameter is determined by the size of the catalytic nanoparticle. This is why spinels are expected to give well-spaced single-walled carbon nanotubes (SWNTs) and multi-walled carbon nanotubes (MWNTs) of controllable diameters within a 20 nm range [79]. $NiAl_2O_4$, $CoAl_2O_4$, and $ZnFe_2O_4$ were investigated for the growth of SWNTs and MWNTs and few-layer graphene (FLG) by Memon et al. [79]. Low-temperature growth of CNTs at 500 °C occurs for $NiAl_2O_4$ and $CoAl_2O_4$, whereas a high growth temperature of 750 °C is required for $ZnFe_2O_4$.

Photocatalytic Activity and Mechanisms of Oxide Spinels

Photocatalysis procedure includes series of chemical reactions that have tremendous effect on the surroundings [80]. These reactions occur between materials (catalysts) and medium with the aid of irradiation that is usually in the range of ultraviolet and visible light. Such irradiation causes excitations of the atoms of the medium causing a yield of electrons (e-) and hole (h+) pairs which are involved in further chemical reactions that form radical oxygen species (ROS) [81]. These radicals are known to have the most influence in the surroundings such as degradation of dyes [82] and acids [83] as well as antibacterial effect [84]. Moreover, the (e−/h+) pairs can cause several reactions and produce H_2 which is considered as an excellent resource of energy [85]. There are many factors affecting the efficiency of the photocatalysis including the power of the irradiation [86], the chemical [87] and physical [88] nature of the medium, and the choice of catalyst material [89].

Many materials are subjected to photocatalysis experiment [90]. The choice of these materials depends on the morphology and characteristics of the materials [91]. For an efficient photocatalysis procedure, large surface area is required because of its major effect on the surroundings [92]. The optical properties are very important too, as a good irradiation absorber is required to have an adequate band gap energy to efficiently absorb radiation [93]. Also, heterogeneous structure is essential to provide higher rate of ions production, usually semiconductors are used [94]. The addition of dopant and noble metals has shown an incredible effect on the photocatalyst activity [95]. Considering all of the above, nanoparticles (NPs), in particular oxides, emerged as excellent candidates for photocatalysis [96] owning to the unique controllable structure [97] and enhanced surface area [98] as well as enhanced optical properties

Fig. 14 (continued) CNT4 = $MgFe_2O_4$ (1100 °C); CNT5 = $MgFe_2O_4$ (1200 °C)). The (ID/IG) ratio is presented in the box; (**b**) histogram of the diameter distribution of MWNTs in the sample CNT4, at the left side, TEM images of the produced MWNTs with $MgFe_2O_4$ as catalyst; (**c**) resulting 3D CNT macrostructure (Reprinted from [78], Copyright (2017), with permission from Elsevier)

[99]. Herein, we discuss the recent studies involving oxide NPs in photocatalytic reactions for the degradation of dyes, degradation of acids, hydrogen production, and antibacterial activity. These studies include in-depth characterization (morphological and optical properties) of NPs using several techniques such as scanning electron microscopy (SEM), transmission electron microscopy (TEM), X-ray diffraction (XRD), Fourier-transform infrared spectroscopy (FTIR), energy-dispersive X-ray spectroscopy (EDS), and diffuse reflectance spectroscopy (DRS). Characterization was directly associated to the performance of the examined samples as efficient photocatalysts.

Degradation of Dyes

Dyes are known as one of the most chemical compounds used in industry [100] and found excessively in wastewater causing dangerous consequences to the nature surroundings [101]. Therefore, wastewater treatment attempts to clear these pollutant dyes from water through degradation that can be achieved as a result of photocatalytic reactions [82, 102–115]. Table 5 shows the most used dyes in photocatalysis experiments. The efficiency of the degradation can be estimated by the following simple equation:

$$\text{Effeciency } (\%) = \frac{C_0 - C}{C_0} \times 100$$

where C_0 and C are the concentrations of the dye in the water before and after photocatalysis process, respectively.

Oxides spinel NPs are considered as excellent candidates for photocatalysis, because transition metal spinel structure provided yield of ions at their octahedral sites that exchange with the tetrahedral sites which enhances photocatalytic activity. $CuCo_2O_4$ prepared through hydrothermal method reveal flowerlike nanorods (Fig. 15a), with a BET surface area of 30.13 m^2/g. A complete degradation of MO dye was achieved within 240 min (Fig. 15b) under simulated solar light irradiation [102]. Photochemical measurements confirmed the high charge separation and hence efficient photocatalytic activity [102].

Visible light was applied to assess the catalytic activity of $ZnFe_2O_4$ NPs synthesized by chemical route [103]. Cubic spinel structure was confirmed by XRD with crystallite size ranging from 15 to 30 nm. TEM showed spherical agglomerated grains (Fig. 16a). The prepared NPs were then applied as a photocatalyst for the degradation of Orange II dye in different experimental parameters varying in pH of the medium (3,6,7.9), power of the visible light source (35, 70, 150, and 250 W), and the concentration of the catalyst (0.1, 0.2, 0.3, 0.4, 0.5, 1 g/L). It was observed that the efficiency of the degradation was the highest at pH 6 (94.9%) and then drops to 71.5% with more alkaline medium (pH 9). This was explained by the reaction of H_2O groups and OH-radicals in alkaline medium that affect negatively the generation of ROS and hence lower the rate of photocatalytic activity [103].

Table 5 Typical types of dyes found in waste water and are applied in photocatalysis and degradations experiments

Congo red	Methyl orange	Rhodamine B	Methylene Blue	Orange II
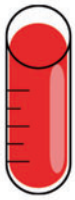			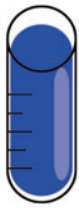	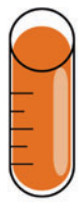
CR	**MO**	**RhB**	**MB**	**Orange II**

Moreover, as the power increased from 35 to 250 W, the efficiency of the photocatalysis raised dramatically from 71.2% to 94.9% (Fig. 16b). This is due to the increase of the ionization rate and hence more (e^-/h^+) pairs are generated. The effect of the concentration of $ZnFe_2O_4$ powder was confirmed too, as increasing the concentration from 0.1 to 0.5 g/L raised dramatically the efficiency from 40.7% to 94.9%, respectively. This verifies the major effect of $ZnFe_2O_4$ as an efficient photocatalyst for the degradation of Orange II dye [103].

Oxides are well known by their unique shapes and smaller size resulting in higher surface area and hence potential candidates for photocatalytic applications. Flower-like Co_3O_4 NPs synthesized by subsequent thermal treatment showed high photocatalytic activity for the degradation of different dyes RhB under UV-vis light. TEM showed nanoflowers with pore size around 7.6 nm. Degradation studies showed that the proposed Co_3O_4 NPs were the most efficient with RhB as 100% of the dye was degraded in 60 min [104].

Also, a facile hydrothermal route was applied to form 3D $ZnCo_2O_4$ marigold flower used as catalyst for the degradation of MB dye under visible light source. SEM showed flower-shaped NPs with sizes in the range 3–5 μm with petals having much smaller sizes in the range 40–50 nm [82].

Oval-shaped agglomerated $SrFe_2O_4$ NPs were prepared by ultrasonic assisted sol-gel were investigated for the degradation of MB dye under visible light. The rugby-shaped NPs have grain size ranging from 20 to 30 nm (Fig. 17a). The efficiency of photocatalysis reached 78% in 180 min. This degradation was further improved by combining the spinel oxide with reduced graphene oxide (RGO) resulting in much higher efficiency of 98.41% (Fig. 17b). However, the reproducibility of the catalytic reaction was found to be affected with repeated cycles, as the degradation decreases from 98.41% to 81.75% after 4 h (four cycles). This was probably due to some byproducts that reduce the generation of ROS, especially that the crystal structure was confirmed to be stable during these four cycles [105].

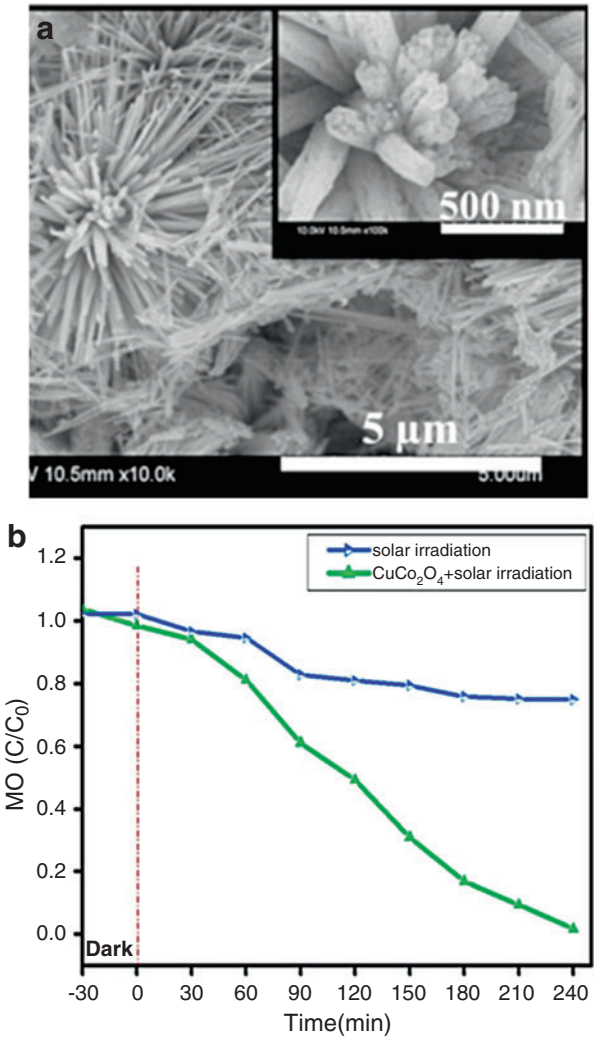

Fig. 15 (**a**) SEM images and high-resolution SEM image in the inset of urchin-like $CuCo_2O_4$ nanostructure; (**b**) the C/C_0 versus irradiation time curve of degradation of MO (Reprinted from [102], Copyright (2017), with permission from Elsevier)

Reduced graphene oxide (RGO) was also combined with $ZnFe_2O_4$ in different ratios of RGO (0.2, 0.4, 0.6, and 0.8) (Fig. 18a). The maximum photocatalytic activity was achieved with the ratio of 0.4, while, when different pH mediums were examined (1, 3, 7, and 9), the maximum RhB degradation activity was found at pH = 1. At low pH, the oxidation process is enhanced which in turns increase the formation of ROS [106]. The stability of the reaction was studied too showing a sharp decrease in the degradation efficiency within five cycles (Fig. 18b) [106].

Composites containing spinel oxides with other materials showed excellent photocatalysis activity for the degradation of MO dye. Coupled g-C_3N_4 and $ZnAl_2O_4$ prepared by conventional calcination method resulted in pure high crystalline gC_3N_4/Al_2O_4 composite as confirmed by XRD. SEM and TEM showed a

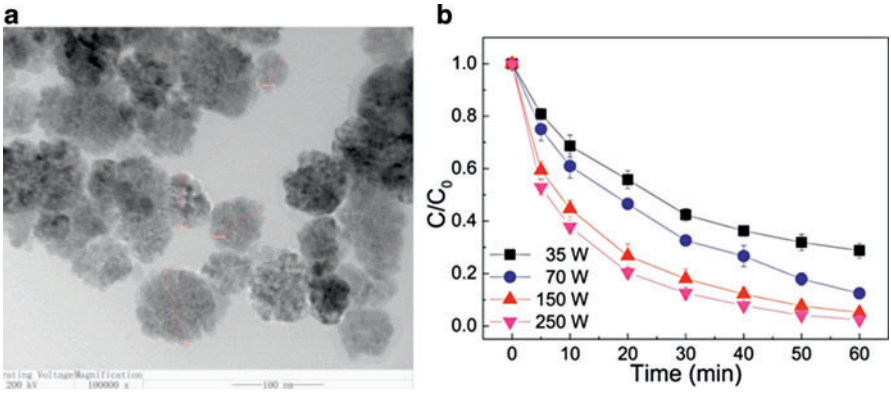

Fig. 16 (**a**) Typical TEM images at high magnification of fresh $ZnFe_2O_4$ powders; (**b**) decolorization of Orange II under effect of different visible light power (Reprinted from [103], Copyright (2016), with permission from Elsevier)

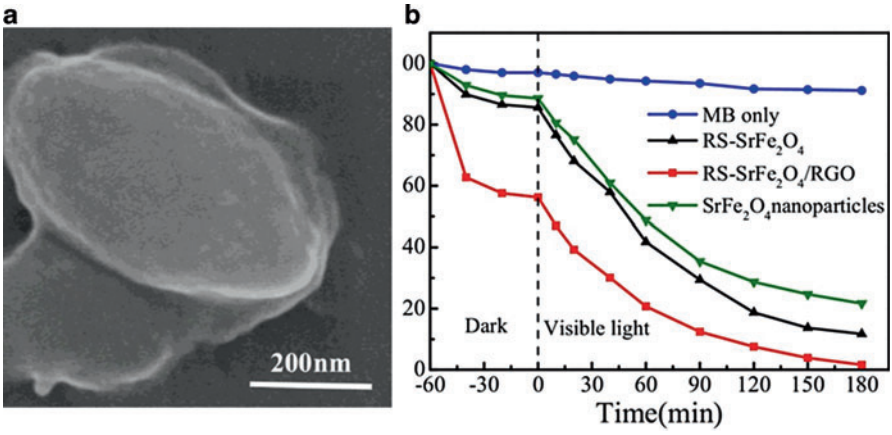

Fig. 17 (**a**) SEM of $SrFe_2O_4$ combined with RGO. (**b**) Photocatalytic degradation of MB with different catalysts (Reprinted from [105], Copyright (2016), with permission from Elsevier)

typical aggregated morphology with larger particle size (200–500 nm). This combination resulted in efficient degradation of MO dye under visible light (94% in 2 h) when compared with g-C_3N_4 (70%) and $ZnAl_2O_4$ (10%) separately. This confirmed the role of heterogeneous medium in increasing (e^-/h^+) pairs resulting in enhanced generation of ROS that cause the degradation of the dye. Cycling tests of MO dye degradation showed good reproducibility as the degradation efficiency reduced very slightly with time [107].

The great benefit due to the combination of graphene and spinel is also confirmed for rGO/$MgFe_2O_4$ composites prepared through hydrothermal process resulting in enhanced photocatalysis activity for the degradation of MB dye under visible light.

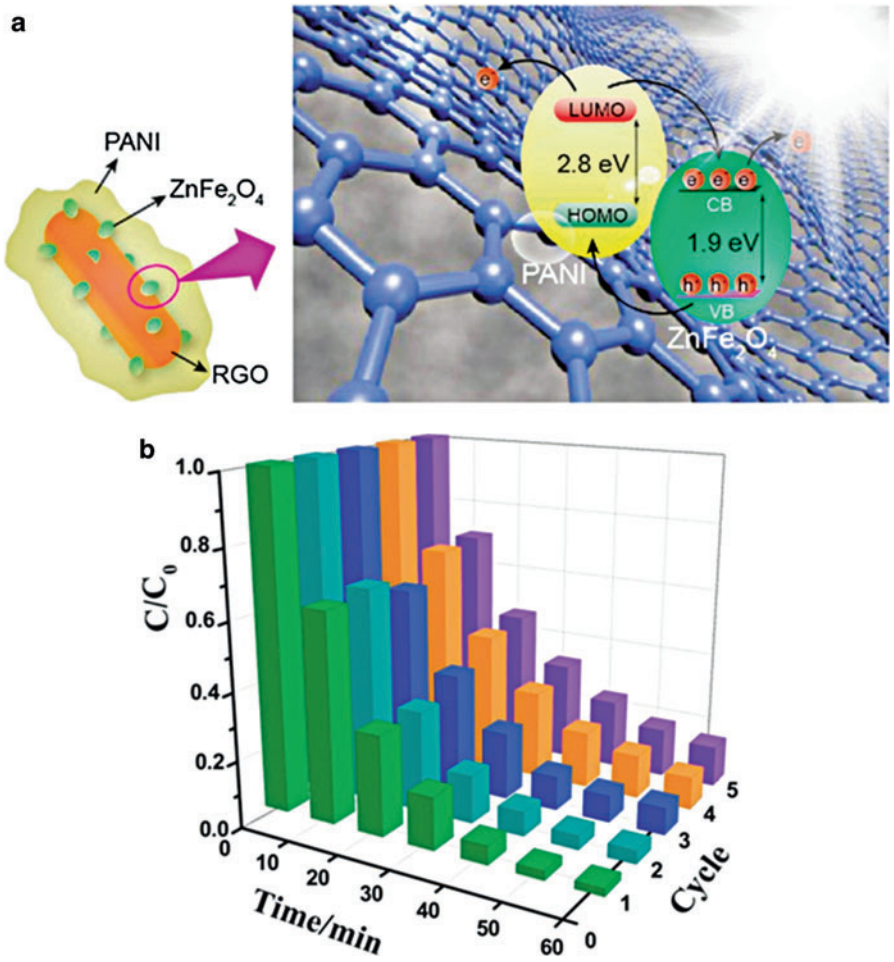

Fig. 18 (**a**) The microstructure and photocatalytic mechanism diagram of $ZnFe_2O_4$ with RGO photocatalyst; (**b**) the photodegradation of RhB behavior for five cycles with $ZnFe_2O_4$ with RGO ration of 0.2 (Reprinted from [106], Copyright (2016), with permission from Elsevier)

XRD and FTIR confirmed the formation of pure cubic spinel phase of $MgFe_2O_4$, while Raman spectroscopy confirmed the purity of the prepared composites with complete reduction of graphite oxide into graphene. Uniform spherical-shaped grains were observed by SEM, while magnetic measurements revealed a ferromagnetic behavior. UV-visible spectra showed good absorbance in the visible light region, and accordingly, photocatalysis experiments indicated significant enhancement of the degradation efficiency of MB dye (100% in 25 min) compared with $MgFe_2O_4$ alone (25% in 25 min). This shows the importance of combining an excellent light absorber such as $MgFe_2O_4$ with rGO that plays an important role in increasing charge (e^-/h^+) separation (inhibiting recombination) which boosts the photocatalytic activity [108].

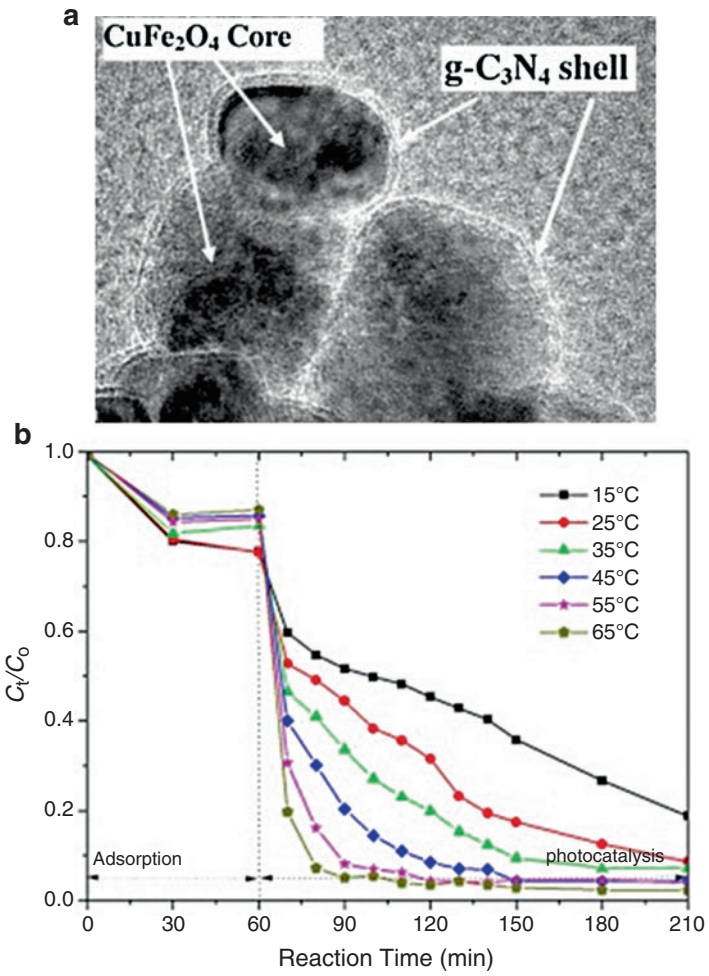

Fig. 19 (**a**) HRTEM images with $CuFe_2O_4@C_3N_4$; (**b**) temperature effects for the photocatalytic degradation of Orange II over $CuFe_2O_4@C_3N_4$ (Reprinted from [109], Copyright (2015), with permission from Elsevier)

Another nanocomposite consisting of core-shell $CuFe_2O_4@C_3N_4$ with different mass ratios (1:1, 1:2, 1:3, 2:1, and 3:1) was prepared through self-assembly method. g-C_3N_4 (graphitic carbon nitride) and $CuFe_2O_4$ phases were confirmed by XRD analysis, while the purity of the chemical composition was confirmed through FTIR. Optical properties (absorption) studied using UV-vis DRS showed absorption in UV-vis light region of 200–800 nm. FESEM images confirmed the core-shell nanostructure (Fig. 19a) of 50–60-nm-sized $CuFe_2O_4$ NPs coated with 5–7 nm shell of g-C_3N_4 film. Photocatalysis experiment for Orange II degradation showed that the highest degradation rate (98% in 120 min) was achieved with (2:1). The effect of medium

temperature and pH were investigated too. It was found that the temperature of the solution affects the degradation efficiency as the highest temperature (65 °C) resulted the best degradation efficiency (98% in 120 min) among other tested temperatures (15, 25, 35, 45, and 55 °C) (Fig. 19b). This was due to the excess of energy at higher temperatures that enhance ROS generation. It was also observed that the degradation efficiency increases at certain pH (8.75 and 9.12). This was explained by the presence of HCO_3^- and Cl^- ions at the mentioned pH which lead to further production of radicals that play a major role in the oxidation process during the degradation of Orange II dye [109].

Spinel oxide NPs were also combined with noble metals such as Au and Ag to achieve surface plasmon resonance (SPR) effect that causes the accumulation of ions on the surface of particles and hence strengthening the photocatalytic activity. Co_3O_4 thin films were synthesized through chemical route and coated with Au NPs with spin coating processing. XRD confirmed pure Au/Co_3O_4 composites loosely agglomerated of 50–100 nm were noticed in SEM images (Fig. 20a). The degradation of Congo red (CR) dye was investigated using different percentage of Au coating ($x = 0$, 5, 10, 20, 30, 40, 50, and 60% mol) under visible light irradiation. It was revealed that the maximum degradation occurred at 40% mol of Au. The degradation efficiency (C/C_0) was shown to increase gradually from 48% at 5% mol of Au to 81% at 40% mol of Au. Further increase of Au percentage resulted in noticeable decrease in CR degradation efficiency (Fig. 20b). Absorption spectra showed that the maximum SPR peak is correlated with 40% Au (Fig. 20c). As SPR effect was found to increase with the amount of Au distributed uniformly around the spinel oxide Co_3O_4. However, for the highest Au loading, an increase of particle aggregation was noticed, hence reducing the uniformity and active sites (surface area) of Au which diminish the SPR effect and hence the degradation efficiency [110].

Other work attempted combining SPR effect with heterogeneous composite resulting in high-efficient degradation process. Ag-$ZnFe_2O_4$ were loaded in different amount of reduced grapheme oxide (rGO) (20, 40, 80, and 100 mg) through microwave-assisted self-assembly precipitation method. The degradation process was performed by varying several experimental parameters. In terms of grapheme oxide amount, the maximum degradation rate was achieved with rGo 80 and 100 mg reaching 100% degradation efficiency of MB in only 30 min. Other dyes (MO and RhB) were tested too with 80 mg rGo samples giving efficiencies of 70% and 95%, respectively, in 30 min. The as-obtained results showed that the photocatalysis activity is the most efficient with MB dyes. Also, UV irradiation showed better degradation than visible light. This confirms that the type of irradiation influences the excitation rate and hence the photocatalytic activity. Reusability tests indicated an excellent stability of the degradation process of MB dye as no change was noticed over five cycles [111].

Furthermore, a recent study showed how spinel ferrite $CoFe_2O_4$ could actually improve the photocatalytic activity of AgBr NPs for the degradation of MO dye [112]. $CoFe_2O_4$ NPs were synthesized through hydrothermal method and then combined with AgBr through facile precipitation-deposition method with

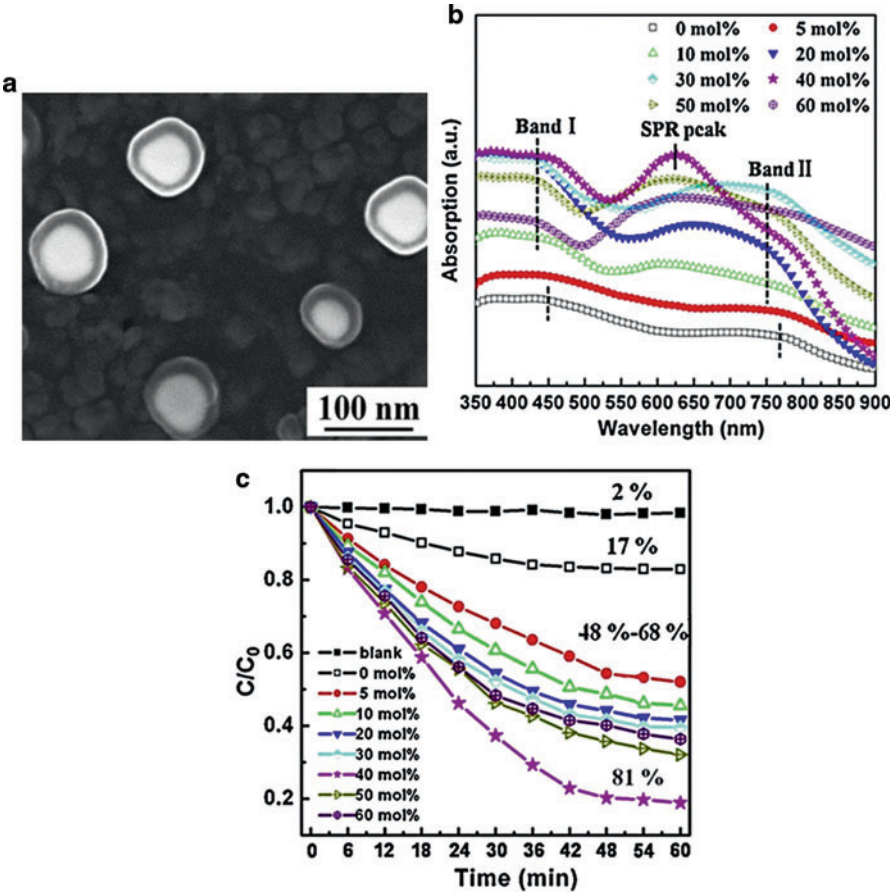

Fig. 20 (**a**) SEM top view image of Au/Co_3O_4. (**b**) Degradation rate of CR calculated from its absorption intensity variation. (**c**) Optical absorption spectra of Co_3O_4 and Au/Co_3O_4 thin films with various Au contents (Reprinted from [110], Copyright (2013), with permission from Elsevier)

different weights of $CoFe_2O_4$ to AgBr (5, 10, and 20%). XRD patterns showed sharp peaks of all samples indicating the purity and crystallite phase stability. Microspheres of (0.1–0.6 μm) of AgBr were formed with $CoFe_2O_4$ NPs having sizes in the range 20–60 nm distributed through the microspheres (Fig. 21a). Photocatalytic experiments under visible light revealed that increasing the content of $CoFe_2O_4$ NPs on the surface of AgBr microspheres from 5% to 20% increased the removal of MO dye from 80% to 90% in 40 min, respectively (Fig. 21b). It was also proved that the degradation of MO dye is much more efficient with less initial concentrations of MO. The pH influence was confirmed too, as the best efficiency was achieved with pH 4 indicating that the degradation of MO is more efficient in an acidic condition as it has an anionic configuration. In general, for an efficient degradation, the pH of the medium should be appropriate with the chemical nature of the chosen dye in order to

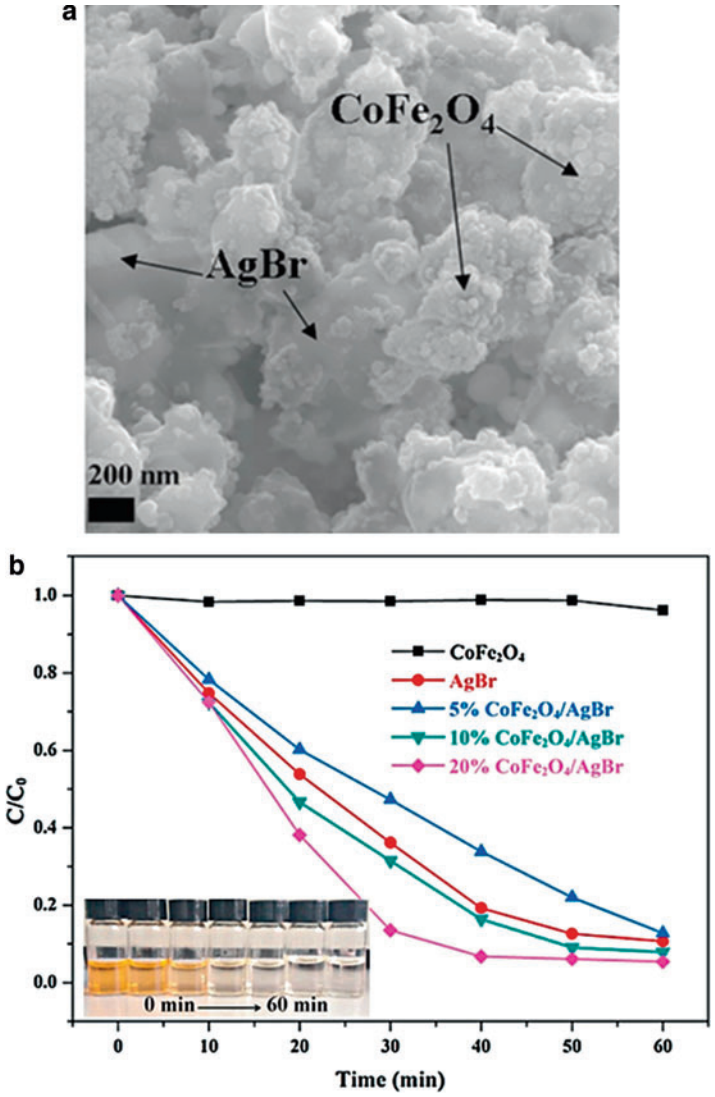

Fig. 21 (**a**) SEM image of $CoFe_2O_4$ with 10% Ag Br. (**b**) Photodegradation of MO (10 mg/L) by the different catalysts at pH 7 (the inset is the photos of MO solutions after photocatalytic degradation by the 20%$CoFe_2O_4$/AgBr composite) (Reprinted from [112], Copyright (2017), with permission from Elsevier)

create higher yield of radicals in the medium that are the main cause of degradation [112]. This study further investigated the pH and dye relation as the prepared 20% $CoFe_2O_4$ NPs were used as a photocatalyst for the degradation of other dyes (RhB and MB) under different pH values. It was shown that the degradation behavior of the three tested dyes is different for the same pH. At pH 7, 92% of RhB were

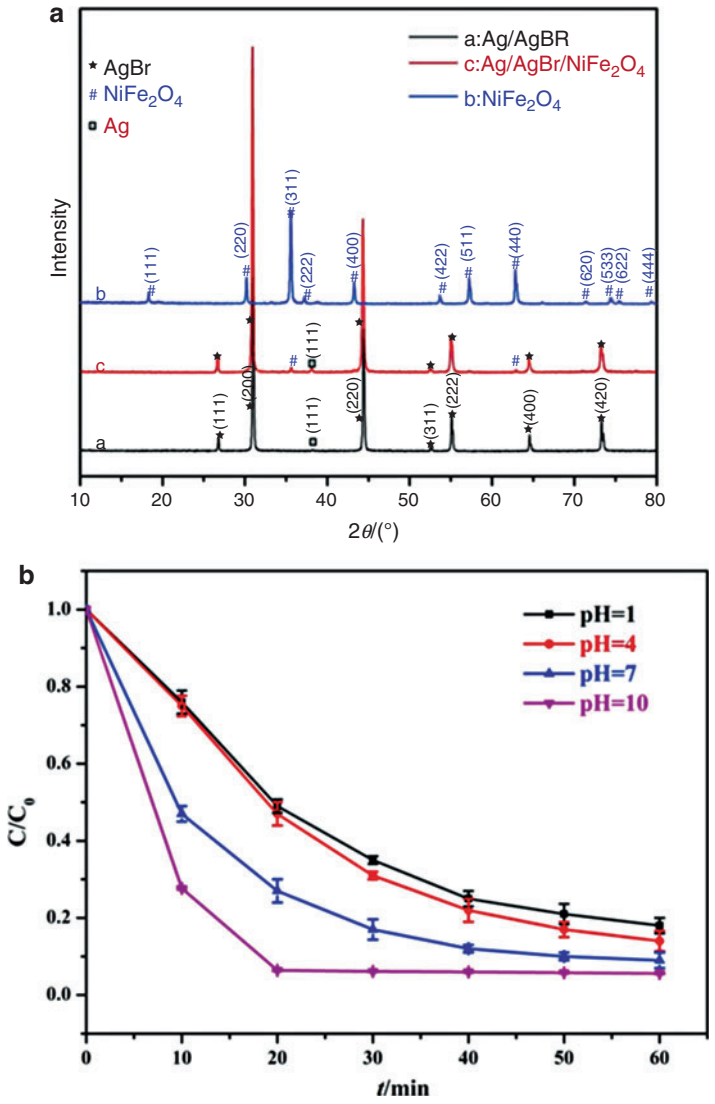

Fig. 22 (**a**) XRD patterns of the as-obtained photocatalysts. (**b**) Photodegradation of RhB (10 mg/L) over $Ag/AgBr/NiFe_2O_4$ plasmonic photocatalyst at different pH values (Reprinted from [113], Copyright (2017), with permission from Elsevier)

degraded in 20 min, whereas only 26% of MB was removed in 60 min and 90% of MO in 40 min. By only changing the pH to 10, MB degradation reached 80% in 60 min [112].

A recent study introduced a nanocomposite of $Ag/AgBr/NiFe_2O_4$ synthesized through hydrothermal route as an efficient photocatalyst for RhB degradation under visible light. The crystalline structure of the composite was confirmed by XRD

analysis, while the elemental composition was determined by XPS (Fig. 22a). Photocatalysis experiment showed a degradation efficiency of 89% in only 6 min (Fig. 22b). The change of pH showed a dramatic effect on the degradation process of RhB; the degradation ability of the composite is enhanced with increasing pH value. This was correlated to the cationic nature of RhB as it could be easily absorbed at pH 7 and 10. The degradation efficiency was found to be higher for the mixed composite giving a k value of 0.0402 min^{-1} higher than Ag/AgBr (0.0348 min^{-1}) and $NiFe_2O_4$ (0.0015 min^{-1}) [113].

Zr-doped NiCo-ferrite ($Zr_xCo_{0.8-x}Ni_{0.2-x}Fe_2O_4$) and graphene nanocomposites were prepared through co-precipitation method followed by annealing at 750 °C for 6.5 h. Pure cubic spinel phase was confirmed by XRD with an average grain size of 100 nm. The composite of mixed spinels showed an excellent degradation of MB (100% in 35 min) under visible light at $x = 0.06$ [91].

Spinel oxides were also mixed with other oxides in order to achieve high-performance photocatalytic activity by creating heterogeneous medium. A composite of SnO_2/Zn_2SnO_4 was prepared through hydrothermal method forming rod and flakelike nanoparticles showed high photocatalysis activity, reaching a degradation rate of almost 99% of MO dye in 30 [114].

Moreover, heterogeneous structure of two spinel oxides has a remarkable photocatalysis performance for the degradation of dyes. A mixed composite of Co_3O_4 and Ag_3PO_4 which are p-type and n-type semiconductors, respectively, were prepared through precipitation method. SEM images revealed unique 3D smooth surface tetrapod microcrystals of Ag_3PO_4 where Co_3O_4 NPs were attached to their surface (Fig. 23a). Such structure provides a high surface area (5.104 m^2/g) which is essential for a successful photocatalytic process. A schematic diagram of the photocatalysis process is illustrated in Fig. 23b showing the role of Ag molecules in SPR effect that further enhances the activity of the photocatalyst. Applying the prepared samples of 2% wt Co_3O_4/Ag_3PO_4 as a photocatalyst under visible light for the degradation of MB dye has shown excellent results as 100% of the MB dye was degraded in 12 min only in comparison with 24 min for Ag_3PO_4 alone. Though Ag_3PO_4 is considered as a good photocatalyst due to the presence of Ag particles that cause SPR effect, adding the cubic spinel Co_3O_4 on its surface would further increase the surface area and also create a heterogamous structure that enhance absorption of light as well as separation of electrons and holes which indeed enhance photocatalysis. It was also found that the photocatalytic efficiency is greatly dependent on the amount of Co_3O_4 as 2% was found to be the optimum content percentage (Fig. 23c). Higher contents (3% wt) resulted in less efficient activity. This was explained by the "shielding effect" where higher amounts of Co_3O_4 NPs start covering the absorption active sites on Co_3PO_4 liming the absorption of irradiated light and hence reducing the efficiency of the process [115].

Degradation of Acids

Most of chemical compounds used in daily life contain dangerous acids that end their path in wastewater causing side effects on health and environment. Oxide NPs

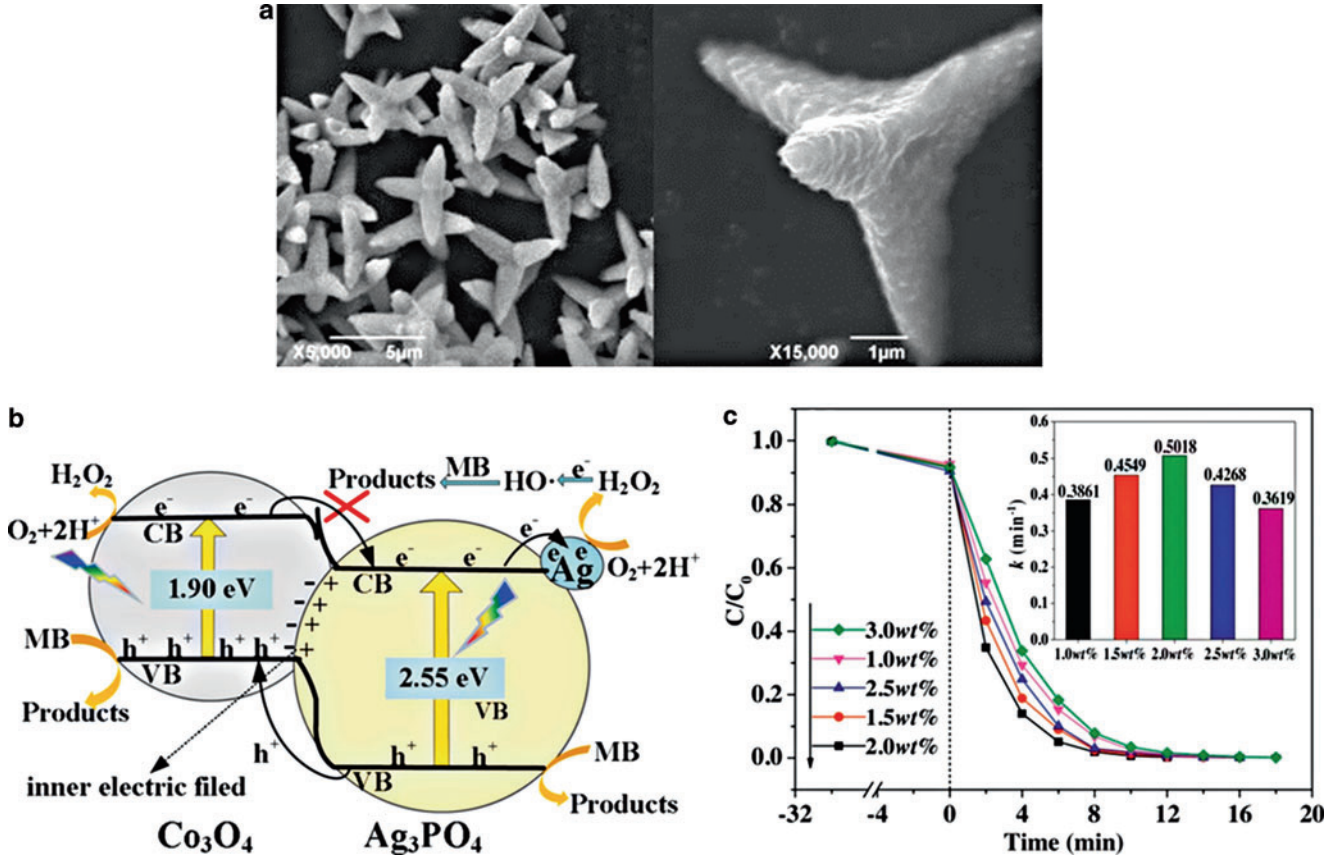

Fig. 23 (**a**) SEM images of 2 wt% Co_3O_4/Ag_3PO_4. (**b**) Photocatalytic mechanism scheme of the Co_3O_4/Ag_3PO_4 composite. (**c**) Photocatalytic degradation curves of MB over samples: (**a**) Co_3O_4/Ag_3PO_4 composites with different Co_3O_4 content calcined at 673 K (Reprinted from [115], Copyright (2016), with permission from Elsevier)

emerged as a good solution of destruction these acids remnants in wastewater. The degradation of acids through photocatalysis by oxide NPs is considered as a good water treatment method, so water can be reused in wider applications such as cleaning and agriculture [116].

Ternary zinc oxides including $ZnAl_2O_4$, $ZnFe_2O_4$, and Zn_2SnO_4 prepared by different synthesis routes were examined for the degradation of phenol molecules through photocatalysis process under solar irradiation XRD confirmed the formation of spinels with cubic structure, having crystallite size 7.3, 15.79, and 17.1 nm for $ZnAl_2O_4$, $ZnFe_2O_4$, and Zn_2SnO_4, respectively. FTIR verified the bonding between the active sites (octahedral and tetrahedral), while isotherm adsorption-desorption technique gave the specific areas 158.10, 58.96, and 42.91 m^2/g for $ZnAl_2O_4$, $ZnFe_2O_4$, and Zn_2SnO_4, respectively, in agreement with the crystallite size change (as smallest particles result in larger specific area). This is a very important factor that influences the efficiency of the photocatalytic process. When applying only sunlight, without catalyst, no considerable degradation of phenol was observed, while a noticeable degradation was found when the prepared samples were introduced as photocatalyst confirming the major effect of NPs in the photocatalysis process and giving the maximum efficiency of 100% in 240 min for Zn_2SnO_4 [117].

$ZnCo_2O_4$-doped ZrO_2 NPs prepared by hydrothermal co-precipitation and subjected to calcinations under various temperatures (250–550 °C) were applied in photocatalysis for the degradation of 2-chlorophenol acid in wastewater. The results showed that the prepared $ZnCo_2O_4$ NPs own relatively high surface area (262.3 m^2/g), which even increased with ZrO_2 doping to 534 m^2/g after calcination at 350 °C. However, with higher calcination temperatures, the surface area decreases to 439.5 m^2/g at 550 °C. XRD showed a pure crystalline spinel phase with clear crystal growth with calcinations temperature (from 16 to 47 nm), which explains the decrease in surface area. SEM images confirmed the crystal growth too. Adsorption experiment performed in dark showed a maximum adsorption of 14% with samples calcined at 350 °C. On the other hand, the photocatalysis experiment showed enhanced efficiency in the degradation of the 2-chlorophenol acid for all prepared samples under visible light and medium pH of 5. The sample calcined at 350 °C caused the maximum degradation of 70% in 180 min. It was also shown that increasing the amount of catalyst from 0.5 to 1 g will increase the degradation to from 45% to 70% in 180 min. In addition, when the medium is more acidic (pH = 3), the degradation increased rapidly to 90% in 90 min [118].

A combination of Cu_2O and Co_3O_4 NPs was found to be effective in the degradation of phenol as well as MB dye. Heterogeneous disoriented nanorods of Co_3O_4 of around 450 nm diameter were decorated with different amounts of Cu_2O quantum dots (7, 5, and 3 wt %) (Fig. 24a). The degradation of phenol was examined under various conditions in potassium monopersulfate triple PMS medium. Light experiment showed no degradation of phenol as well as introducing Co_3O_4 NPs. It is important to mention here that Co_3O_4 NPs have a considerable effect in the degradation of MB dye, much more that in phenol which was almost nil. Interestingly, the degradation efficiency of phenol increased considerably when the prepared mixed composite of Cu_2O/Co_3O_4 were used (Fig. 24b). This was also found to be affected

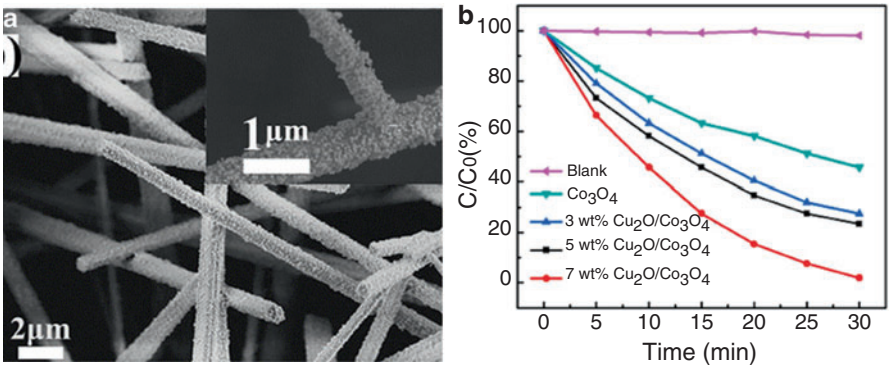

Fig. 24 (**a**) SEM images of the Co_3O_4 nanorods with Cu_2O QDs 7 wt% coating with a high-magnification inset. (**b**) Time-dependent degradation efficiency of MB assisted with PMS (Reprinted from [119], Copyright (2016), with permission from Elsevier)

by the amount of Cu_2O; it increased from 70% to 100% in 30 min, when the amount increased 3–7 wt%, respectively. Experiments were performed in another medium too (H_2O_2) giving similar results of maximum degradation efficiency for 7% wt CuO_2/Co_3O_4. With both systems (PMS and H_2O_2), the prepared nanocomposites showed great reproducibility over five cycles. This was further confirmed by SEM as images taken for the 7% wt Cu_2O/Co_3O_4 catalyst after the photocatalysis process were very similar to those taken after, showing the large stability of the composites [119].

Hydrogen Production

One of the important outcomes of photocatalytic reactions is the production of hydrogen (H_2), usually, under solar spectrum, which is considered as an effective, reproducible, and clean way to generate energy [120]. For an efficient H_2 production by photocatalysis, a heterogeneous catalysis is required to provide high photosensitization and large catalysis active sites for high electrons production [120]. During photocatalysis chemical reactions, oxidation process creates electrons that are responsible of coupling protons H^+ (reduction) to get hydrogen atoms (H_2) [121].

Ferrites of $NiFe_{2-x}Mn_xO_4$ (x = 0.0, 0.4, 0.6, 0.8, 1.2, 1.6, and 2.0) have been prepared by sol-gel route, with a cubic structure confirmed by XRD and TEM (Fig. 25a). The crystallite size from XRD was found to decrease (from 38 to 31 nm) for small Ni content (x <0.4) and then increased gradually (31–63 nm) for higher Ni content (x = 0.4–2.0). This was confirmed by TEM too, as the agglomerated cubic grains were seen to increase in size from with Mn content. Therefore, the surface area was found to be decreased from 36 to 18 m^2/g (x = 0.4–2.0), while the calculated energy band gap was found to decrease from 1.56 to 1.09 eV (x = 0.4–2.0). All prepared samples were tested for H_2 production. The effect of

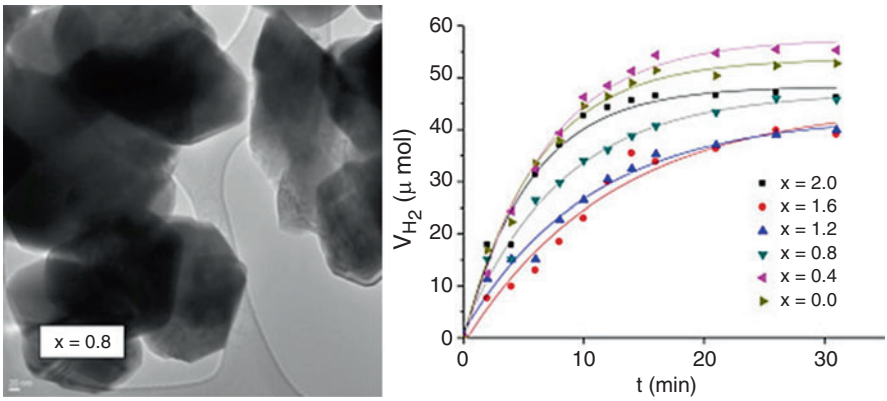

Fig. 25 (**a**) TEM micrographs of $NiFe_{2-x}Mn_xO_4$ prepared by sol-gel. (**b**) Volume of evolved H_2 versus illumination time for the $NiFe_{2-x}Mn_xO_4$ system ($0 \leq x \leq 2$) (Reprinted from [122], Copyright (2015), with permission from Elsevier)

surface area was the dominant factor in this study, as the maximum H_2 evolution was obtained with the sample with smallest crystallite size (31 nm) and the largest surface (36 m^2/g) with $x = 0.4$ (Fig. 25b). Its energy band gap of 1.53 eV is relatively large compared with the smallest value of 1.09 eV for $x = 2$. The effect of medium pH was confirmed in this study as H_2 evolution was found to be enhanced in basic medium (pH = 9.4) as oxidation process is promoted and hence more H_2 [122].

Moreover, zinc ferrite with formula $A_{0.2}Zn_{0.8}Fe_2O_4$ (A = Co, Ni, and Cu) prepared by precipitation, followed by annealing with 650 °C for 2 h, was examined for H_2 evolution. XRD peaks confirmed the formation of crystalline pure spinel phase with crystallite size varying from 12.3 nm for Cu to 27.3 for pure $ZnFe_2O_4$. Hence, BET surface areas varied in accordance to the crystallite size giving maximum value of 53 m^2/g for the smallest crystallite size obtained for $Cu_{0.2}Zn_{0.8}Fe_2O_4$. The band gap varied from 1.78, 1.89, and 2.07 for Co, Ni, and Cu, respectively. Photocatalysis experiments performed in NaOH electrolyte solution gave the maximum H_2 evolution for Co (650 μmol/g). This was related to the narrower band gap (1.78 eV) and the higher electrical conductivity ($14.5 \times 10^7\ \Omega^{-1}\ cm^{-1}$ at 600 K) determined for $Co_{0.2}Zn_{0.8}Fe_2O_4$, making it the best catalyst among (Ni and Cu) related spinels, though the latter has much larger surface area and the band gap and electrical conductivity were found to control the reaction [123].

Oxides of $InGaO_3(ZnO)_m$ (m = 1, 2, 3, and 4) were modified with different amounts of CuO and NiO (1, 2, 4, and 10 wt%). XRD analysis showed only peaks related to $InGaO_3(ZnO)_m$ phase, with no peaks of CuO and NiO, thereby confirming their fine distribution in the lattice. Band gap varied from 3.6 to 3 eV at $m = 2$ and 4, respectively [124].

Spinels of MAl_2O_4 (M = Mg, Sr, and Ba) as well as $MgAl_2O_4/Al_2O_3$ composite prepared by solid-state method were recently applied for H_2 production through photocatalysis procedure coupled with gas chromatographic equipment. XRD confirmed the formation of pure phase; meanwhile SEM showed agglomerated grains

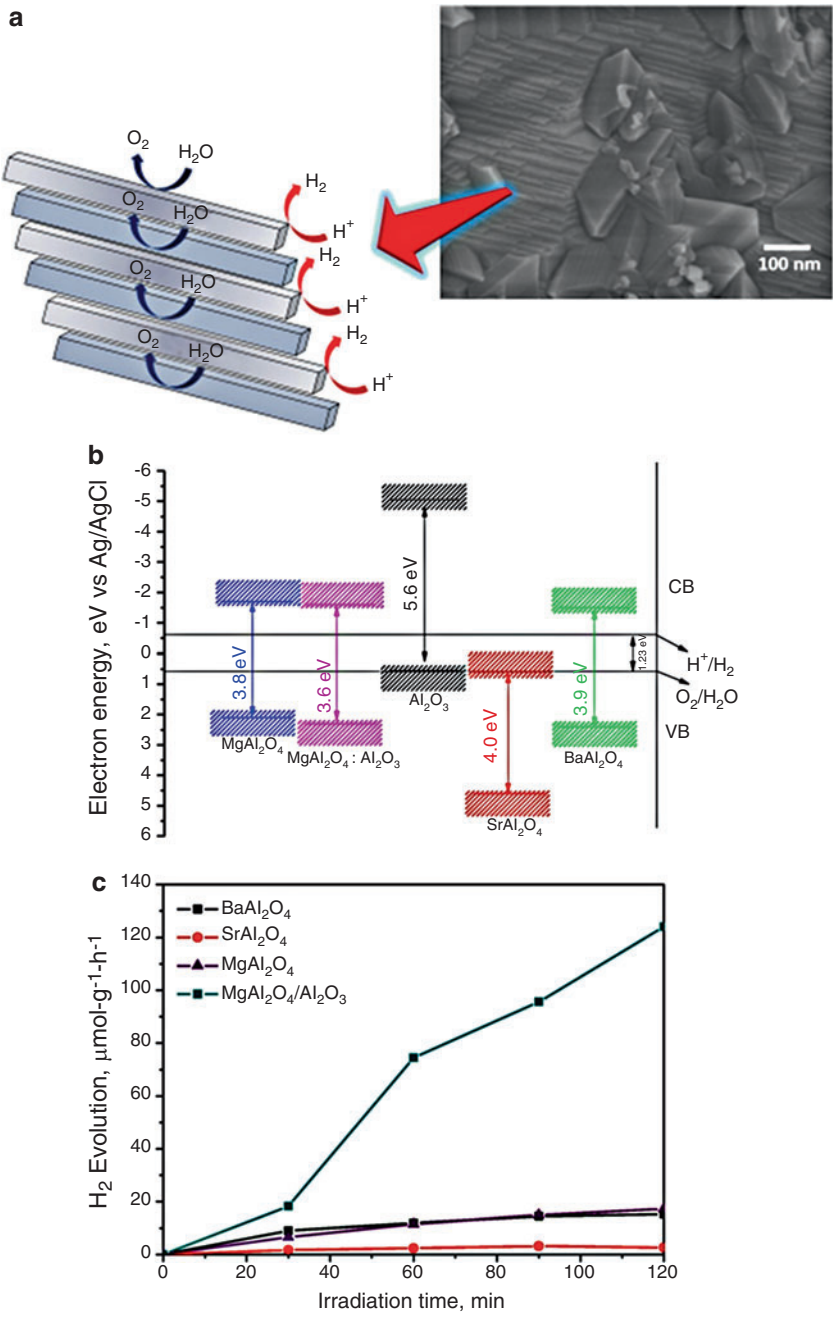

Fig. 26 (**a**) SEM images for $MgAl_2O_4/Al_2O_3$, showing the formation of steps. (**b**) Illustration of the electronic band structure for $MgAl_2O_4$, $SrAl_2O_4$, $BaAl_2O_4$, and $MgAl_2O_4/Al_2O_3$. (**c**) Photocatalytic hydrogen production using $MgAl_2O_4$, $SrAl_2O_4$, $BaAl_2O_4$, and $MgAl_2O_4/Al_2O_3$ as photocatalysts (Reprinted from [125], Copyright (2017), with permission from Elsevier)

with size variation with M, giving the largest grain with $BsAl_2O_4$ (2 μm). With the composite $MgAl_2O_4/Al_2O_3$, the grain size dropped to the nanosize sheets of 10–20 nm showing the presence of Al_2O_3 (Fig. 26a). This would favor the generation of nanosize particles and hence increases the surface area that is essential for efficient photocatalysis process because of the increase of the active sites. The band gap calculated from the absorbance spectra obtained from UV-vis DRS varied in the range from 3.6 to 4.0 eV for $MgAl_2O_4/Al_2O_3$ and $SrAl_2O_4$ (Fig. 26b). Therefore, the effect of grain size and the band gap was shown clearly in the photocatalysis results. The maximum H_2 production rate was obtained with $MgAl_2O_4/Al_2O_3$ (120 μmol/g after 2 h) (Fig. 26c), which has the highest surface area and the lowest band gap [125].

Uniform smooth surface cubic-shaped spinel oxides of $CuGa_{2-x}Fe_xO_4$ ($x = 0.8$, 0.6, and 0.4) were synthesized by ceramic route and confirmed by SEM and XRD. The size decreased with x. These samples were applied in photocatalysis experiment in sulfate medium to measure the H_2 evolution under visible light and pH 12. It was found that the H_2 production varied with x too, giving the maximum evolution of (10,045 mmol/h) with $CuGa_{1.6}Fe_{0.4}O_4$. The H_2 is produced through the chemical reactions occurring through photocatalysis which produces yield of ion pairs (hole and electrons) [121]. Here the electrons are responsible to reduce the protons to hydrogen through the following chemical reactions:

$$H_2S + OH^- \overset{pH=12}{\rightarrow} HS^- + H_2O$$

$$2HS^- + 2h^+ \rightarrow S^{2-} + 2H^+$$

$$2H^+ + 2e^- \rightarrow H_2$$

Furthermore, CNTs decorated with oxides were found to have good H_2 evolution during photocatalysis. $ZnFe_2O_4$ were prepared through hydrothermal route and hence accompanied with CNTs in different weights of 0, 0.5, 1.0, 3.0, and 5.0 wt %. TEM showed clearly the distribution of $ZnFe_2O_4$ on CNTs (Fig. 27a). Phase stability and chemical composition were confirmed by XRD and EDS, while Eg was calculated using UV-vis DRS spectra. Photocatalytic experiments were performed in methanol solution along with PL measurements confirming carrier separation. From (Fig. 27a), it can be seen clearly that no H_2 evolution was detected with CNTs only, while combining it with ZFe_2O_4 gave a considerable H_2 evolution that increased with CNTs giving the maximum evolution (18 μmol of H_2) at CNTs 1 wt %. However, with more CNTs, the evolution started decreasing to 7.5 μ mol at CNTs 5 wt% (Fig. 27b). This is because at certain CNT amount, the opacity and light scattering will start disturbing photocatalytic reactions, reducing the amount of (h+/e−) pairs. Figure 27c illustrates the mechanism of photocatalysis for H_2-production with the presence of CNTs [126].

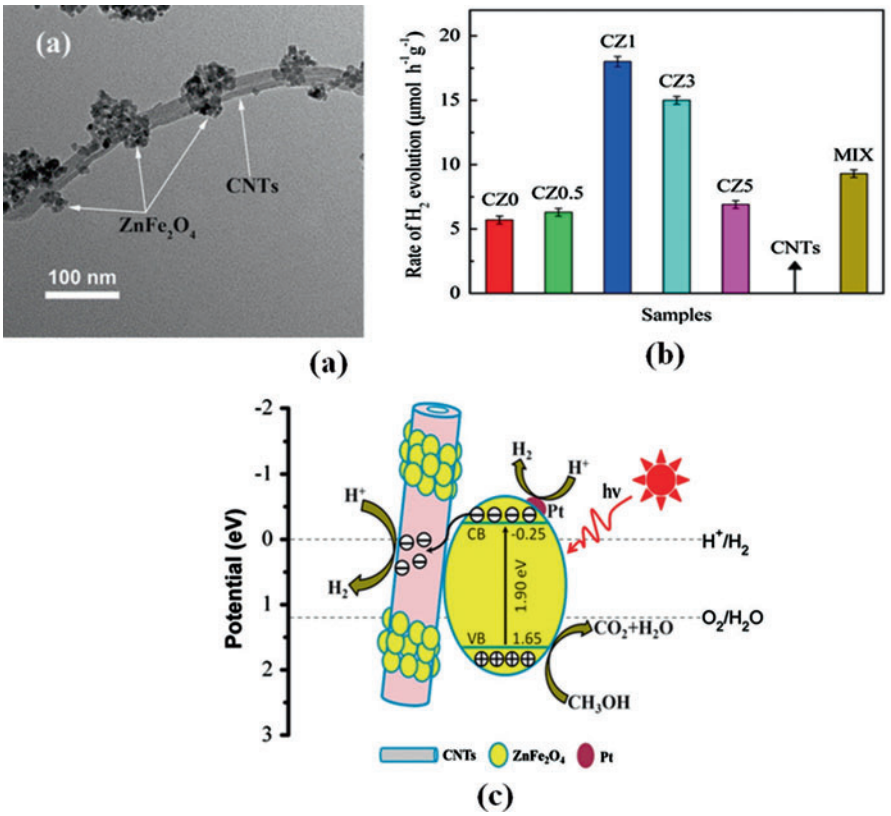

Fig. 27 (**a**) TEM image of 1.0 wt% CNTs/$ZnFe_2O_4$. (**b**) Comparison of the photocatalytic H_2 production activity over different photocatalysts under the employed conditions of 10 vol% methanol aqueous solution and 400 W high-pressure Hg lamp irradiation, where MIX is the physical mixture of CNTs and $ZnFe_2O_4$, (**c**) proposed photocatalytic H_2 evolution mechanism for CNTs/$ZnFe_2O_4$ composite under high-pressure Hg lamp irradiation (Reprinted from [126], Copyright (2016), with permission from Elsevier)

Antibacterial Activity

As a result of photocatalysis chemical reactions, beside degradation and energy generation, some effect was found on bacteria, raising an additional benefit of the process [127]. ROS generated during photocatalysis reactions can affect the cellular life and interrupt the bacterial growth and even cause bacterial death [84]. Oxide NPs have shown to have a considerable antibacterial activity along with photocatalysis [128]. Beta-silver molybdate (β-Ag_2MoO_4) was applied as a photocatalyst in three different mediums, pH = 8.5, PVP, and ethanol under visible light (Fig. 28a). It is clearly shown from TEM images in Fig. 28a that the morphology of β-Ag_2MoO_4 crystals was strongly affected by the change of the chemical environment, and hence the photocatalytic behavior was different too. Antibacterial activity for *E. coli* was

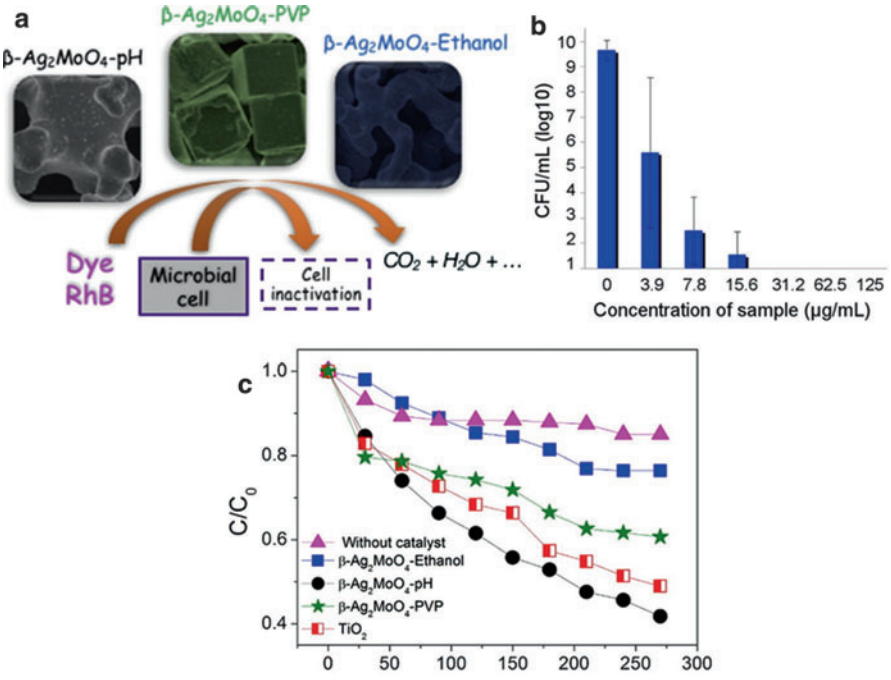

Fig. 28 (**a**) Schematic diagram showing the TEM of β-Ag_2MoO_4 in three different mediums and the results of photocatalytic process. (**b**) Mean values of log10 (CFU/mL) of planktonic cultures of *E. coli* exposed to β-Ag_2MoO_4-Ethanol. Errors bars: standard deviation (**c**) photocatalysis degradation profiles of RhB with β-Ag_2MoO_4crystals (Reprinted from [128], Copyright (2017), with permission from Elsevier)

examined by determining bacterial growth as well as the bacterial acid concentrations that indicated bacterial death. Bacterial inhibition was found in all mediums with the maximum inhibition rate related to ethanol medium, indicating that the medium has big influence on the bacterial death (Fig. 28b). The bacterial inhibition was explained by the formation of superoxide ion (O_2'), OOH* radicals and hydrogen ions (H), which resulted in e− and h+ interactions. This will cause protein inactivation and consequently cell death. On the other hand, the maximum degradation of RhB dye was related to the pH medium (Fig. 28c). This was related to the carbon presence during the photocatalysis process that differ between mediums ranging from 0.06% for pH medium to 0.91% for ethanol medium which accordingly affected the RhB degradation rate [128].

Moreover, spinel NPs of $Mn_{1-x}Ni_xFe_2O_4$ (x = 0, 0.1, 0.2, 0.3, 0.4, and 0.5) prepared by microwave combustion method were examined for antibacterial activity during photocatalysis [129]. Morphology and characterization of the samples were deeply examined through several techniques showing pure cubic spinel phase crystals varying in size with $x = 0.1$ to $x = 0.5$ from 16 to 72 nm. Owning excellent

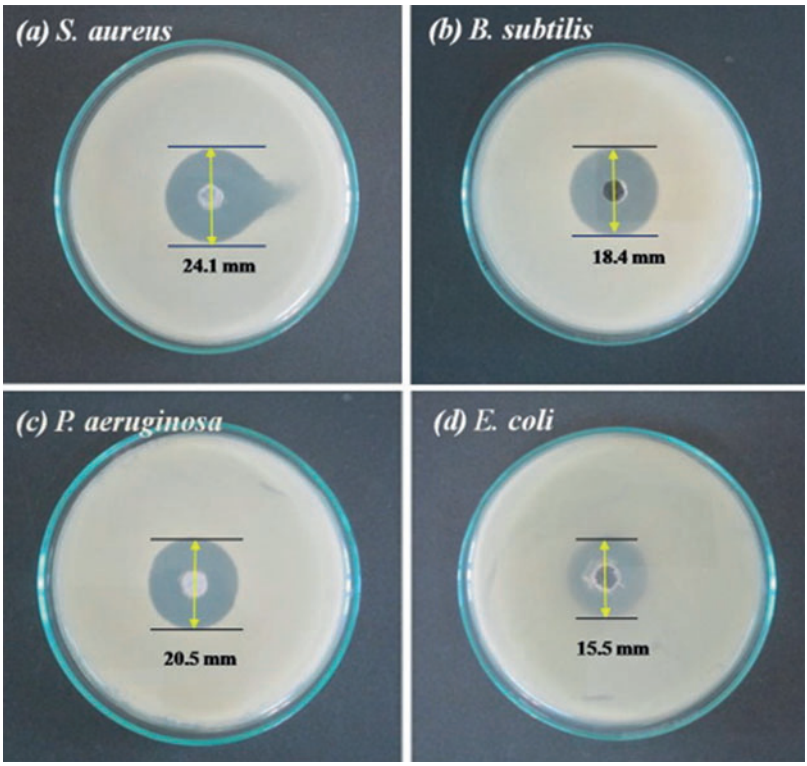

Fig. 29 Zone of inhibition produced by $Mn_{0.5}Ni_{0.5}Fe_2O_4$ nanoparticles against the bacterial strains (**a**) *Staphylococcus aureus*, (**b**) *Bacillus subtilis*, (**c**) *Pseudomonas aeruginosa*, and (**d**) *E. coli* (Reprinted from [129], Copyright (2016), with permission from Elsevier)

optical properties with band gap values ranging from 1.56 to 1.83 eV corresponding to $x = 0$ and $x = 0.5$. The inhibition rate was measured for four different bacteria species (*Staphylococcus aureus*, *Bacillus subtilis*, *Pseudomonas aeruginosa*, and *E. coli*). The size of the inhibition zone was measured in the bacterial culture under microscope (Fig. 29). It was found that the maximum inhibition occurs when the sample of $x = 0.5$ was applied. This was associated to the morphology of the sample as the crystallite size was decreasing with increasing the amount of Ni atoms (increasing x) giving the smallest value of 16 nm for $x = 0.5$ sample [129].

Conclusions

This chapter summarized the different approaches in the researches devoted to modify the catalytic properties of different oxide spinels by affecting their surface structure. The presented data illustrates how the cationic distribution and method of synthesis of spinel catalysts determine the resulting catalytic properties and

performances. More researches are needed for the developed of novel nanocomposites containing spinel oxides combined with other materials (such as graphene, zeolites, MOFs), as well as better clarify the mechanisms involved during photocatalysis process.

References

1. Coïsson M, Barrera G, Celegato F et al (2017) Hysteresis losses and specific absorption rate measurements in magnetic nanoparticles for hyperthermia applications. Biochim Biophys Acta Gen Subj 1861(6):1545–1558. https://doi.org/10.1016/j.bbagen.2016.12.006
2. Satalkar M, Kane SN, Kumaresavanji M et al (2017) On the role of cationic distribution in determining magnetic properties of $Zn_{0.7-x}Ni_xMg_{0.2}Cu_{0.1}Fe_2O_4$ nano ferrite. Mater Res Bull 91:14–21. https://doi.org/10.1016/j.materresbull.2017.03.021
3. Kane SN, Satalkar M (2017) Correlation between magnetic properties and cationic distribution of $Zn_{0.85-x}Ni_xMg_{0.05}Cu_{0.1}Fe_2O_4$ nano spinel ferrite: effect of Ni doping. J Mater Sci 52:3467. https://doi.org/10.1007/s10853-016-0636-7
4. Ahmed MA, Hassan HE, Eltabey MM et al (2018) Mössbauer spectroscopy of $Mg_xCu_{0.5-x}Zn_{0.5}Fe_2O_4$ (x = 0.0, 0.2 and 0.5) ferrites system irradiated by γ-rays. Physica B: Cond Matt 530:195–200. https://doi.org/10.1016/j.physb.2017.10.125
5. Tatarchuk TR, Paliychuk ND, Bououdina M et al (2018) Effect of cobalt substitution on structural, elastic, magnetic and optical properties of zinc ferrite nanoparticles. J Alloys Compd 731:1256–1266. https://doi.org/10.1016/j.jallcom.2017.10.103
6. Tatarchuk T, Bououdina M, Macyk W et al (2017) Structural, optical, and magnetic properties of Zn-doped $CoFe_2O_4$ nanoparticles. Nanoscale Res Lett 12(1):141–151. https://doi.org/10.1186/s11671-017-1899-x
7. Kurta SA, Mykytyn IM, Tatarchuk TR (2014) Structure and the catalysis mechanism of oxidative chlorination in nanostructural layers of a surface of alumina. Nanoscale Res Lett 9(1):357–365. https://doi.org/10.1186/1556-276X-9-357
8. Liu Y, Hsu J, Fu Y et al (2016) Preparation of Cu–Zn ferrite photocatalyst and it's application. Int J Hydrog Energy 41(35):15696–15702. https://doi.org/10.1016/j.ijhydene.2016.04.127
9. Karthik K, Dhanuskodi S, Gobinath C et al (2017) Photocatalytic and antibacterial activities of hydrothermally prepared CdO nanoparticles. J Mater Sci Mater Electron 28:11420–11429. https://doi.org/10.1007/s10854-017-6937-z
10. Reddy DHK, Yun YS (2016) Spinel ferrite magnetic adsorbents: alternative future materials for water purification? Coord Chem Rev 315:90–111. https://doi.org/10.1016/j.ccr.2016.01.012
11. Yang MH, Jeong JM, Lee KG et al (2017) Hierarchical porous microspheres of the Co_3O_4@graphene with enhanced electrocatalytic performance for electrochemical biosensors. Biosens Bioelectron 89:612–619. https://doi.org/10.1016/j.bios.2016.01.075
12. Zhao M, Fan S, Liang J (2015) Synthesis of mesoporous grooved $ZnFe_2O_4$ nanobelts as peroxidase mimetics for improved enzymatic biosensor. Ceram Int 41(9):10400–10405. https://doi.org/10.1016/j.ceramint.2015.04.080
13. Ahmad T, Bae H, Iqbal Y, Rhee I et al (2015) Chitosan-coated nickel-ferrite nanoparticles as contrast agents in magnetic resonance imaging. J Magn Magn Mater 381:151–157. https://doi.org/10.1016/j.jmmm.2014.12.077
14. Kombaiah K, Vijaya JJ, Kennedy JL et al (2018) Okra extract-assisted green synthesis of $CoFe_2O_4$ nanoparticles and their optical, magnetic, and antimicrobial properties. Mater Chem Phys 204:410–419. https://doi.org/10.1016/j.matchemphys.2017.10.077
15. Abdel-Hamid Z, Rashad MM, Mahmoud SM et al (2017) Electrochemical hydroxyapatite-cobalt ferrite nanocomposite coatings as well hyperthermia treatment of cancer. Mater Sci Eng C 76:827–838. https://doi.org/10.1016/j.msec.2017.03.126

16. Wang G, Zhao D, Ma Y et al (2018) Synthesis and characterization of polymer-coated manganese ferrite nanoparticles as controlled drug delivery. Appl Surf Sci 428:258–263. https://doi.org/10.1016/j.apsusc.2017.09.096
17. Sohrabnezhad S, Rezaeimanesh M (2017) Synthesis and characterization of novel magnetically separable $NiFe_2O_4$@AlMCM-41-Cu_2O core-shell and its performance in removal of dye. Adv Powder Technol 28(11):3039–3048. https://doi.org/10.1016/j.apt.2017.09.014
18. Jacobs JP, Maltha A, Reintjes JGH (1994) The surface of catalytically active spinels. J Catal 147:294–300
19. Briceño S, Castillo HD, Sagredo V (2012) Structural, catalytic and magnetic properties of $Cu_{1-X}Co_XFe_2O_4$. Appl Surf Sci 263:100–103. https://doi.org/10.1016/j.apsusc.2012.09.007
20. Védrine JC (2014) Revisiting active sites in heterogeneous catalysis: their structure and their dynamic behaviour. Appl Cat A Gen 474:40–50. https://doi.org/10.1016/j.apcata.2013.05.029
21. Li X, Zhu K, Pang J (2018) Unique role of Mössbauer spectroscopy in assessing structural features of heterogeneous catalysts. Appl Catal B Environ 224:518–532. https://doi.org/10.1016/j.apcatb.2017.11.004
22. Liu K, Rykov AI, Wang J (2015) Chapter one – recent advances in the application of Mößbauer spectroscopy in heterogeneous catalysis. In: Jentoft FC (ed) Advances in catalysis, vol 58. Academic, San Diego, pp 1–142. https://doi.org/10.1016/bs.acat.2015.09.001
23. Bauminger R, Cohen SG, Marinov A et al (1961) Study of the low-temperature transition in magnetite and the internal fields acting on iron nuclei in some spinel ferrites, using Mössbauer absorption. Phys Rev 122:1447
24. Kelly WH, Folen VJ, Hass M et al (1961) Magnetic field at the nucleus in spinel-type crystals. Phys Rev 124:80
25. Evans BJ, Hafiner SS, Kalvius GM (1966) The hyperfine fields of ^{57}Fe at the A and B sites in copper ferrite ($CuFe_2O_4$). Phys Lett 23:24–25
26. Evans BJ (1968) Magnetic hyperfine interactions in some spinel ferrites. In: Proceedings of the fourth symposium on mossbauer effect methodology, Chicago, Illinois, England Nuclear Corporation. Plenum Press, New York, pp 139–158
27. Sicafus KE, Wills JM, Grines NW (1999) Structure of spinel. J Am Ceram Soc 82:3279–3292
28. Da Dalt S, Takimi AS, Volkmer TM et al (2011) Magnetic and Mossbauer behavior of the nano structured $MgFe_2O_4$ spinel obtained at low temperature. Powder Technol 210:103–108
29. Abbas YM, Mansour SA, Ibrahim MME et al (2011) Microstructure characterization and cation distribution of nanocrystalline cobalt ferrite. J Magn Magn Mater 323:2748–2756
30. Sepelak V, Becker KD (2004) Comparison of the nanoscale milled spinel ferrites with that of the quenched bulk materials. Mater Sci Eng A 375–377:861–864
31. Naik PP, Sali RBT, Meena SS et al (2014) Gamma radiation roused lattice contraction effects investigated by Mossbauer spectroscopy in nanoparticles Mn-Zn Ferrite. Radiat Phys Chem 102:147–152
32. Deraz NM (2008) Production and characterization of pure and doped copper ferrite nanoparticles. J Anal Appl Pyrolysis 62:212–222
33. Rana MU, Islam M, Abbas T (2000) Cation distribution and magnetic interactions in Zn-substituted $CuFe_2O_4$ ferrites. Mater Chem Phys 65:345–349
34. Heiba ZK, Mohamed MB, Hamdeh HH et al (2015) Structural analysis and cation distribution of nanocrystalline $Ni_{1-x}Zn_xFe_{1.7}Ga_{0.3}O_4$. J Alloys Compd 618:755–760
35. Lakhani UK, Pathak TK, Vasoya NH et al (2011) Structural parameters and X-ray Debye temperature determination study on copper ferrite aluminates. Solid State Sci 13:539–547
36. Heiba ZK, Mohamed MB, Ahmed MA et al (2014) Cation distribution and dielectric properties of nanocrystalline gallium substituted nickel ferrite. J Alloys Compd 586:77–781. https://doi.org/10.1016/j.jallcom.2013.10.137
37. Dhal GC, Mohan D, Prasad R (2017) Preparation and application of effective different catalysts for simultaneous control of diesel soot and NO_X emissions: an overview. Cat Sci Technol. https://doi.org/10.1039/C6CY02612E

38. Lin X, Li S, He H et al (2017) Evolution of oxygen vacancies in MnOx-CeO2 mixed oxides for soot oxidation. Appl Catal B. https://doi.org/10.1016/j.apcatb.2017.06.071
39. Legutko P, Jakubek T, Kaspera W et al (2014) Soot oxidation over K-doped manganese and iron spinels – how potassium precursor nature and doping level change the catalyst activity. Catal Commun 43:34–37. https://doi.org/10.1016/j.catcom.2013.08.021
40. Legutko P, Kaspera W, Stelmachowski P et al (2014) Boosting the catalytic activity of magnetite in soot oxidation by surface alkali promotion. Catal Commun 56:139–142. https://doi.org/10.1016/j.catcom.2014.07.020
41. Liu H, Dai X, Wang K et al (2017) Highly efficient catalysts of $Mn_{1-x}Ag_xCo_2O_4$ spinel oxide for soot combustion. Catal Commun 101:134–137. https://doi.org/10.1016/j.catcom.2017.08.007
42. Fino D, Russo N, Saracco G et al (2008) Removal of NO_x and diesel soot over catalytic traps based on spinel-type oxides. Powder Technol 180(1–2):74–78. https://doi.org/10.1016/j.powtec.2007.03.003
43. Zawadzki M, Staszak W, López-Suárez FE et al (2009) Preparation, characterisation and catalytic performance for soot oxidation of copper-containing $ZnAl_2O_4$ spinels. Appl Catal A General 371(1–2):92–98. https://doi.org/10.1016/j.apcata.2009.09.035
44. Liu Z, Zhou Z, He F (2017) Catalytic decomposition of N_2O over NiO-CeO_2 mixed oxide catalyst. Catal Today 293–294:56–60. https://doi.org/10.1016/j.cattod.2017.02.030
45. Kapteijn F, Rodriguez-Mirasol J, Moulijn JA (1996) Heterogeneous catalytic decomposition of nitrous oxide. Appl Catal B Environ 9(1–4):25–64. https://doi.org/10.1016/0926-3373(96)90072-7
46. Pachatouridou E, Papista E, Iliopoulou EF et al (2015) Nitrous oxide decomposition over Al_2O_3 supported noble metals (Pt, Pd, Ir): effect of metal loading and feed composition. J Environ Chem Eng 3(2):815–821. https://doi.org/10.1016/j.jece.2015.03.030
47. Abu-Zied BM, Bawaked SM, Kosa SA et al (2017) Effects of Nd-, Pr-, Tb- and Y-doping on the structural, textural, electrical and N_2O decomposition activity of mesoporous NiO nanoparticles. Appl Surf Sci 419:399–408. https://doi.org/10.1016/j.apsusc.2017.05.040
48. Yu H, Wang X, Wu X et al (2018) Promotion of Ag for Co_3O_4 catalyzing N_2O decomposition under simulated real reaction conditions. Chem Eng J 334:800–806. https://doi.org/10.1016/j.cej.2017.10.079
49. Grzybek G, Stelmachowski P, Gudyka S et al (2015) Insights into the twofold role of Cs doping on deN_2O activity of cobalt spinel catalyst – towards rational optimization of the precursor and loading. Appl Catal B Environ 168–169:509–514. https://doi.org/10.1016/j.apcatb.2015.01.005
50. Ciura K, Grzybek G, Wójcik S et al (2017) Optimization of cesium and potassium promoter loading in alkali-doped Zn0.4Co2.6O4|Al2O3 catalysts for N2O abatement. Reac Kinet Mech Cat 121:645. https://doi.org/10.1007/s11144-017-1188-9
51. Xue L, Zhang C, He H et al (2007) Catalytic decomposition of N_2O over CeO_2 promoted Co_3O_4 spinel catalyst. Appl Catal B Environ 75(3–4):167–174. https://doi.org/10.1016/j.apcatb.2007.04.013
52. Maniak G, Stelmachowski P, Stanek JJ et al (2011) Catalytic properties in N_2O decomposition of mixed cobalt–iron spinels. Catal Commun 15(1):127–131. https://doi.org/10.1016/j.catcom.2011.08.027
53. Rutkowska M, Piwowarska Z, Micek E et al (2015) Hierarchical Fe-, Cu- and Co-Beta zeolites obtained by mesotemplate-free method. Part I: synthesis and catalytic activity in N_2O decomposition. Microporous Mesoporous Mater 209:54–65. https://doi.org/10.1016/j.micromeso.2014.10.011
54. Zhang B, Liu F, He H et al (2014) Role of aggregated Fe oxo species in N_2O decomposition over Fe/ZSM-5. Chin J Catal 35(12):1972–1981. https://doi.org/10.1016/S1872-2067(14)60184-4
55. Boroń P, Chmielarz L, Gurgul J et al (2014) The influence of the preparation procedures on the catalytic activity of Fe-BEA zeolites in SCR of NO with ammonia and N_2O decomposition. Catal Today 235:210–225. https://doi.org/10.1016/j.cattod.2014.03.018

56. Abu-Zied BM, Soliman SA, Abdellah SE (2015) Enhanced direct N_2O decomposition over $Cu_xCo_{1-x}Co_2O_4$ ($0.0 \leq x \leq 1.0$) spinel-oxide catalysts. J Ind Eng Chem 21:814–821. https://doi.org/10.1016/j.jiec.2014.04.017
57. Russo N, Fino D, Saracco G, Specchia V (2007) N_2O catalytic decomposition over various spinel-type oxides. Catal Today 119(1–4):228–232. https://doi.org/10.1016/j.cattod.2006.08.012
58. Yan L, Ren T, Wang X et al (2003) Catalytic decomposition of N_2O over $M_xCo_{1-x}Co_2O_4$ (M = Ni, Mg) spinel oxides. Appl Catal B Environ 45(2):85–90. https://doi.org/10.1016/S0926-3373(03)00174-7
59. Grzybek G, Stelmachowski P, Gudyka S et al (2016) Strong dispersion effect of cobalt spinel active phase spread over ceria for catalytic N_2O decomposition: the role of the interface periphery. Appl Catal B Environ 180:622–629. https://doi.org/10.1016/j.apcatb.2015.07.027
60. Grzybek G, Stelmachowski P, Indyka P et al (2015) Cobalt–zinc spinel dispersed over cordierite monoliths for catalytic N_2O abatement from nitric acid plants. Catal Today 257:93–97. https://doi.org/10.1016/j.cattod.2015.02.022
61. Tatarchuk T, Bououdina M, Vijaya JJ et al (2017) Spinel ferrite nanoparticles: synthesis, crystal structure, properties, and perspective applications. In: Fesenko O, Yatsenko L (eds) Nanophysics, nanomaterials, Interface studies, and applications. NANO 2016. Springer proceedings in physics, vol 195. Springer, Cham. https://doi.org/10.1007/978-3-319-56422-7_22
62. Tatarchuk T (2014) Catalytic oxidation of carbon monoxide on lithium-zinc ferrites with a spinel structure. Ekologia i Technika 22(2):70–75
63. Zhang W, Wu F, Li J et al (2017) Dispersion–precipitation synthesis of highly active nanosized Co_3O_4 for catalytic oxidation of carbon monoxide and propane. Appl Surf Sci 411:136–143. https://doi.org/10.1016/j.apsusc.2017.03.162
64. Ahmad W, Noor T, Zeeshan M (2017) Effect of synthesis route on catalytic properties and performance of Co_3O_4/TiO_2 for carbon monoxide and hydrocarbon oxidation under real engine operating conditions. Catal Commun 89:19–24. https://doi.org/10.1016/j.catcom.2016.10.012
65. Amini E, Rezaei M, Sadeghinia M et al (2013) Low temperature CO oxidation over mesoporous $CuFe_2O_4$ nanopowders synthesized by a novel sol-gel method. Chin J Catal 34(9):1762–1767. https://doi.org/10.1016/S1872-2067(12)60653-6
66. Mobini S, Meshkani F, Rezaei M et al (2017) Synthesis and characterization of nanocrystalline copper–chromium catalyst and its application in the oxidation of carbon monoxide. Process Saf Environ Prot 107:181–189. https://doi.org/10.1016/j.psep.2017.02.009
67. Mobini S, Meshkani F, Rezaei M (2017) Surfactant-assisted hydrothermal synthesis of $CuCr_2O_4$ spinel catalyst and its application in CO oxidation process. J Environ Chem Eng 5(5):4906–4916. https://doi.org/10.1016/j.jece.2017.09.027
68. Lv M, Guo X, Wang Z et al (2016) Synthesis and characterization of Co–Al–Fe non-stoichiometric spinel-type catalysts for catalytic CO oxidation. RSC Adv 6:27052–27059. https://doi.org/10.1039/C6RA02204A
69. Tatarchuk T, Bououdina M, Paliychuk N et al (2017) Structural characterization and antistructure modeling of cobalt-substituted zinc ferrites. J Alloys Compd 694:777–791. https://doi.org/10.1016/j.jallcom.2016.10.067
70. Huš M, Dasireddy VDBC, Štefančič NS et al (2017) Mechanism, kinetics and thermodynamics of carbon dioxide hydrogenation to methanol on Cu/ZnAl2O4 spinel-type heterogeneous catalysts. Appl Catal B Environ 207:267–278. 10.1016/j.apcatb.2017.01.077
71. Ghosh BK, Moitra D, Chandel M et al (2017) CuO nanoparticle immobilised mesoporous TiO_2–cobalt ferrite nanocatalyst: a versatile, magnetically separable and reusable catalyst. Catal Lett 147:1061–1076. https://doi.org/10.1007/s10562-017-1993-9
72. Kumar RT, Selvam NCS, Ragupathi C et al (2012) Synthesis, characterization and performance of porous Sr(II)-added $ZnAl_2O_4$ nanomaterials for optical and catalytic applications. Powder Technol 224:147–154. https://doi.org/10.1016/j.powtec.2012.02.044

73. Kumar RT, Suresh P, Selvam NCS et al (2012) Comparative study of nano copper aluminate spinel prepared by sol–gel and modified sol–gel techniques: structural, electrical, optical and catalytic studies. J Alloys Compd 522:39–45. https://doi.org/10.1016/j.jallcom.2012.01.064
74. Wei Y, Meng W, Wang Y et al (2017) Fast hydrogen generation from $NaBH_4$ hydrolysis catalyzed by nanostructured Co–Ni–B catalysts. Int J Hydrog Energy 42(9):6072–6079. https://doi.org/10.1016/j.ijhydene.2016.11.134
75. Wang Y, Li T, Bai S et al (2016) Catalytic hydrolysis of sodium borohydride via nanostructured cobalt–boron catalysts. Int J Hydrog Energy 41(1):276–284. https://doi.org/10.1016/j.ijhydene.2015.11.076
76. Tomboc GRM, Tamboli AH, Kim H (2017) Synthesis of Co_3O_4 macrocubes catalyst using novel chitosan/urea template for hydrogen generation from sodium borohydride. Energy 121:238–245. https://doi.org/10.1016/j.energy.2017.01.027
77. Akbarnejad HR, Daadmehr V, Rezakhani AT et al (2013) Catalytic activity of the spinel ferrite nanocrystals on the growth of carbon nanotubes. J Supercond Nov Magn 26:429. https://doi.org/10.1007/s10948-012-1758-z
78. Zampiva RYS, Kaufmann Junior CG, Pinto JS et al (2017) 3D CNT macrostructure synthesis catalyzed by $MgFe_2O_4$ nanoparticles – a study of surface area and spinel inversion influence. Appl Surf Sci 422:321–330. https://doi.org/10.1016/j.apsusc.2017.06.020
79. Memon NK, Xu F, Sun G et al (2013) Flame synthesis of carbon nanotubes and few-layer graphene on metal-oxide spinel powders. Carbon 63:478–486. https://doi.org/10.1016/j.carbon.2013.07.023
80. Sherly ED, Vijaya JJ, Selvam NCS et al (2014) Microwave assisted combustion synthesis of coupled ZnO–ZrO_2 nanoparticles and their role in the photocatalytic degradation of 2,4-dichlorophenol. Ceram Int 40:5681–5691
81. Joa W, Kumar S, Isaacs MA et al (2017) Cobalt promoted TiO_2/GO for the photocatalytic degradation of oxytetracycline and Congo red. Appl Catal B Environ 201:159–168
82. Kokane SB, Suryawanshi SR, Sasikala R et al (2017) Architecture of 3D $ZnCo_2O_4$ marigold flowers: influence of annealing on cold emission and photocatalytic behavior. Mater Chem Phys 194:55–64
83. Tsai MT, Chang YS, Liu YC (2017) Photocatalysis and luminescence properties of zinc stannate oxides. J. Ceram Int 43:428–434
84. Huang S, Xu Y, Liu Q et al (2017) Enhancing reactive oxygen species generation and photocatalytic performance via adding oxygen reduction reaction catalysts into the photocatalysts. Applied Catalysis B: Environmental 218:174. https://doi.org/10.1016/j.apcatb.2017.06.030
85. Zhang Y, Zhou X, Zhang F et al (2017) Design and synthesis of Cu modified cobalt oxides with hollow polyhedral nanocages as efficient electrocatalytic and photocatalytic water oxidation catalysts. J Catal 352:246–255
86. Li H, Liu Y, Tang J et al (2016) Synthesis, characterization and photocatalytic properties of $Mg_{1-x}Zn_xAl_2O_4$ spinel nanoparticles. Solid State Sci 58:14–21
87. Zhu HY, Jiang R, Fu YQ et al (2016) Novel multifunctional $NiFe_2O_4$/ZnO hybrids for dye removal by adsorption, photocatalysis and magnetic separation. Appl Surf Sci 369:1–10
88. Xu Y, Aia J, Zhang H (2016) The mechanism of degradation of bisphenol A using the magnetically separable $CuFe_2O_4$/peroxymonosulfate heterogeneous oxidation process. J Hazard Mater 309:87–96
89. Liu P, He H, Wei G et al (2016) Effect of Mn substitution on the promoted formaldehyde oxidation over spinel ferrite: catalyst characterization, performance and reaction mechanism. Appl Catal B Environ 182:476–484
90. Huang Y, Long B, Tang M et al (2016) Bifunctional catalytic material: an ultrastable and high-performance surface defect CeO_2 nanosheets for formaldehyde thermal oxidation and photocatalytic oxidation. Appl Catal B Environ 181:779–787
91. Rasheed A, Mahmood M, Ali U et al (2016) $Zr_xCo_{0.8x}Ni_{0.2x}Fe_2O_4$-graphene nanocomposite for enhanced structural, dielectric and visible light photocatalytic applications. Ceram Int 42:15747–15755

92. Mousavi M, Habibi-Yangjeh A (2017) Novel magnetically separable $gC_3N_4/Fe_3O_4/Ag_3PO_4/Co_3O_4$ nanocomposites: visible-light-driven photocatalysts with highly enhanced activity. Adv Powder Technol 28:1540–1553
93. Butt FK, Cao C, Wan Q et al (2014) Synthesis, evolution and hydrogen storage properties of ZnV_2O_4 glomerulus nano/microspheres: a prospective material for energy storage. Int J Hydrogen Energ 39:7842–7851
94. Kima S, Durand P, Andréa E et al (2017) Enhanced photocatalytic ability of Cu, Co doped Zn Al based mixed metal oxides derived from layered double hydroxides. Colloid Surface A 524:43–52
95. Gan L, Xu L, Qian K (2016) Preparation of core-shell structured $CoFe_2O_4$ incorporated Ag_3PO_4 nanocomposites for photocatalytic degradation of organic dyes. Adv Mater Res Switz 109:354–360
96. Mohamed MM, Ibrahim I, Salama TM (2016) Rational design of manganese ferrite-graphene hybrid photocatalysts: efficient water splitting and effective elimination of organic pollutants. Appl Catal A Gen 524:182–191
97. Qiu XP, Yu JS, Xu HM et al (2016) Interfacial effect of the nanostructured Ag_2S/Co_3O_4 and its catalytic mechanism for the dye photodegradation under visible light. Appl Surf Sci 362:498–505
98. Vijayaraghavan T, Suriyaraj SP, Selvakumar R et al (2016) Rapid and efficient visible light photocatalytic dye degradation using AFe_2O_4 (A = Ba, Ca and Sr) complex oxides. Mater Sci Eng B Adv 210:43–50
99. Zeng Y, Wang Y, Chen J et al (2016) Fabrication of high-activity hybrid $NiTiO_3/g\text{-}C_3N_4$ heterostructured photocatalysts for water splitting to enhanced hydrogen production. Ceram Int 42:12297–12305
100. Wang C, Wang X, Xua B et al (2004) Enhanced photocatalytic performance of nanosized coupled ZnO/SnO_2 photocatalysts for methyl orange degradation. J Photoch Photobio A 168:47–52
101. Wang C, Xua B, Wang X et al (2005) Preparation and photocatalytic activity of $ZnO/TiO_2/SnO_2$ mixture. J Solid State Chem 178:3500–3506
102. Maria S, Jeghan N, Kang M (2017) Facile synthesis and photocatalytic activity of cubic spinel urchin-like copper cobaltite architecture. Mater Res Bull 91:108–113
103. Caia C, Zhang Z, Liu J et al (2016) Visible light-assisted heterogeneous Fenton with $ZnFe_2O_4$ for the degradation of Orange II in water. Appl Catal B Environ 182:456–468
104. Huang J, Ren H, Chen K et al (2014) Controlled synthesis of porous Co_3O_4 micro/nano-structures and their photocatalysis property. Superlattice Microst 75:843–856
105. Zhang D, Zhang L (2016) Ultrasonic-assisted sol-gel synthesis of rugby-shaped $SrFe_2O_4$/reduced graphene oxide hybrid as versatile visible light photocatalyst. J Taiwan Inst Chem E 69:156–162
106. Feng J, Hou Y, Wang X et al (2016) In-depth study on adsorption and photocatalytic performance of novel reduced graphene oxide-$ZnFe_2O_4$ polyaniline composites. J Alloy Compd 681:157–166
107. Zhu Z, Wang Z, Di J et al (2016) Enhanced visible-light photocatalytic properties of $g\text{-}C_3N_4$ by coupling with $ZnAl_2O_4$. Catal Commun 86:86–90
108. Ain N, Shaheen W, Bashir B et al (2016) Electrical, magnetic and photoelectrochemical activity of rGO/$MgFe_2O_4$ nanocomposites under visible light irradiation. Ceram Int 42: 12401–12408
109. Yao Y, Lu F, Zhu Y et al (2015) Magnetic core–shell $CuFe_2O_4@C_3N_4$ hybrids for visible light photocatalysis of Orange II. J Hazard Mater 297:224–233
110. Wang S, Zhang B (2013) SPR propelled visible-active photocatalysis on Au-dispersed Co_3O_4 films. Appl Catal A Gen 467:585–592
111. Mady AH, Baynosa ML, Tuma D et al (2017) Facile microwave-assisted green synthesis of Ag-$ZnFe_2O_4$@rGOnanocomposites for efficient removal of organic dyes under UV- and visible-light irradiation. Appl Catal B Environ 203:416–427

112. Li Z, Ai J, Ge M (2017) A facile approach assembled magnetic $CoFe_2O_4$/AgBr composite for dye degradation under visible light. J Env Chem Eng 5:1394–1403
113. Ge M, Liu W, Hu X et al (2017) Magnetically separable Ag/AgBr/$NiFe_2O_4$ composite as a highly efficient, visible light plasmonic photocatalyst. J Phys Chem Solids 109:1–8
114. Wang J, Li H, Meng S et al (2017) One-pot hydrothermal synthesis of highly efficient SnO_x/Zn_2SnO_4 composite photocatalyst for the degradation of methyl orange and gaseous benzene. Appl Catal B Environ 200:19–30
115. Tanga C, Liu E, Wan J et al (2016) Co_3O_4 nanoparticles decorated Ag_3PO_4 tetrapods as an efficient visible-light-driven heterojunction photocatalyst. Appl Catal B Environ 181:707–715
116. Tezuka K, Kogure M, Shan YJ (2014) Photocatalytic degradation of acetic acid on spinel ferrites MFe_2O_4 (M = Mg, Zn, and Cd). Catal Commun 48:11–14
117. Anchieta CG, Sallet D, Foletto EL et al (2014) Synthesis of ternary zinc spinel oxides and their application in the photodegradation of organic pollutant. Ceram Int 40:4173–4178
118. Rashid J, Barakat MA, Mohamed RM et al (2014) Enhancement of photocatalytic activity of zinc/cobalt spinel oxides by doping with ZrO_2 for visible light photocatalytic degradation of 2-chlorophenol in wastewater. J Photoch Photobio A 284:1–7
119. Qiu XP, Yu JS, Xu HM et al (2016) Interfacial effects of the Cu_2O nano-dots decorated Co_3O_4 nanorods array and its photocatalytic activity for cleaving organic molecules. Appl Surf Sci 382:249–259
120. Hao X, Jin Z, Wang F et al (2015) Behavior of borate complex anion on the stabilities and the hydrogen evolutions of $Zn_xCo_{3-x}O_4$ decorated graphene. Superlattice Microst 82:599–611
121. Preethi V, Kanmani S (2012) Photocatalytic hydrogen production over $CuGa_2L_xFe_xO_4$ spinel. Int J Hydrogen Energ 37:18740–18746
122. Rekhila G, Bessekhouad Y, Trari M (2015) Hydrogen evolution under visible light over the solid solution $NiFe_{2-x}Mn_xO_4$ prepared by sol gel. Int J Hydrogen Energ 40:12611–12618
123. Boudjema A, Popescu I, Juzsakova T et al (2016) M-substituted (M = Co, Ni and Cu) zinc ferrite photo-catalysts for hydrogen production by water photo-reduction. Int J Hydrog Energy 41:11108–11118
124. Narendranath SB, Thekkeparambil SV, George L et al (2016) Photocatalytic H_2 evolution from water–methanol mixtures on $InGaO_3(ZnO)_m$ with an anisotropic layered structure modified with CuO and NiO cocatalysts. J Mol Catal A Chem 415:82–88
125. Gómez-Solís C, Peralta-Arriaga SL, Torres-Martínez LM et al (2017) Photocatalytic activity of MAl_2O_4 (M = Mg, Sr and Ba) for hydrogen production. Fuel 188:197–204
126. Dang H, Qiu Y, Cheng Z et al (2016) Short communication hydrothermal preparation and characterization of nanostructured CNTs/$ZnFe_2O_4$ composites for solar water splitting application. Ceram Int 42:10520–10525
127. Gautam S, Shandilya P, Priya B et al (2017) Superparamagnetic $MnFe_2O_4$ dispersed over graphitic carbons and composite and bentonite as magnetically recoverable photocatalyst for antibiotic mineralization. Sep Purif Technol 172:498–511
128. Oliveira CA, Volanti DP, Nogueira AE et al (2017) Well-designed β-Ag_2MoO_4 crystals with photocatalytic and antibacterial activity. Mater Des 115:73–81
129. Jesudoss SK, Vijaya JJ, Kennedy LJ et al (2016) Studies on the efficient dual performance of $Mn_{1-x}Ni_xFe_2O_4$ spinel nanoparticles in photodegradation and antibacterial activity. J Photochem Photobiol B 165:121–132